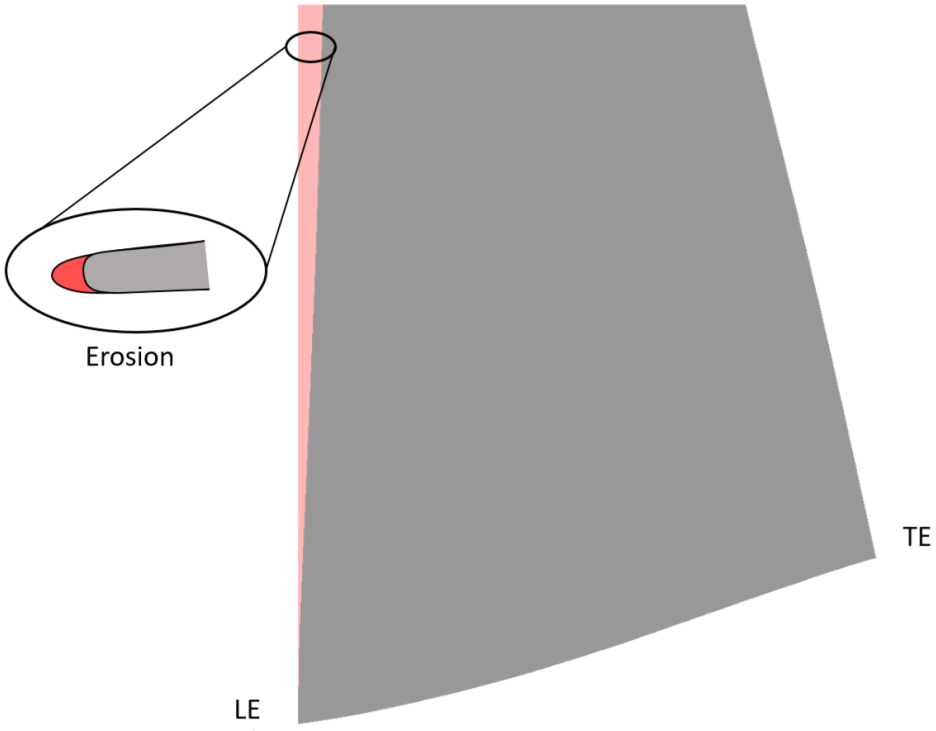

Detection Limits for In-Situ Identification of Damaged Blades

Master's thesis in Mobility engineering

Alexander Boström

DEPARTMENT OF MECHANICS AND MARITIME SCIENCES

CHALMERS UNIVERSITY OF TECHNOLOGY
Gothenburg, Sweden 2025
www.chalmers.se

Master's thesis 2025

Detection Limits for In-Situ Identification of Damaged Blades

ALEXANDER BOSTRÖM

CHALMERS
UNIVERSITY OF TECHNOLOGY

MECHANICS AND MARITIME SCIENCES
Division of Fluid Dynamics
Chalmers University of Technology
Gothenburg, Sweden 2025

Detection Limits for In-Situ Identification of Damaged Blades
ALEXANDER BOSTRÖM

Supervisor: Dr. Marcus Lejon, GKN Aerospace Engine Systems Sweden
Supervisor: Dr. Hans Mårtensson, GKN Aerospace Engine Systems Sweden
Examiner: Prof. Niklas Andersson, Fluid Dynamics, Mechanics and Maritime Sciences

Master's Thesis 2025
Department of Mechanics and Maritime Sciences
Division of Fluid Dynamics
Chalmers University of Technology
SE-412 96 Gothenburg
Telephone +46 31 772 1000

Cover: Wind visualization constructed in Matlab showing a surface of constant wind speed along with streamlines of the flow.

Typeset in LaTeX
Printed by Chalmers Reproservice
Gothenburg, Sweden 2025

Detection Limits for In-Situ Identification of Damaged Blades
ALEXANDER BOSTRÖM
Department of Mechanics and Maritime Sciences
Chalmers University of Technology

Abstract

Over the past decade, axial turbomachinery has seen substantial technological advancements, particularly in improving efficiency and reducing operational costs in aviation. This study investigates the in-situ automatic detection of damage and wear of compressor blades, aiding the enhancement of operational efficiency, reliability, and safety throughout the component lifecycle. The primary objective is to assess the aerodynamic impact of leading-edge erosion on a compressor rotor blade and to determine the detectability limits of such erosion using existing instrumentation in a dedicated experimental test rig.

A series of tests with increasing erosion severity was numerical investigated under both subsonic and transonic flow conditions. Reynolds-Averaged Navier–Stokes (RANS) simulations were performed at multiple operating points at design speed for an experimental rotor blisk , comprising 18 blades. Key flow parameters, including static pressure coefficient, Mach number, and entropy contours, were analyzed to qualitatively and quantitatively evaluate the flow physics.

All test cases exhibited a reduction in polytropic efficiency, with the most significant drop—2.17 percentage points—observed near stall under transonic conditions. Flow field alterations due to erosion included increased profile losses, enhanced tip-leakage effects, and changes in shock structures in transonic regimes. The current sensor configuration in the experimental rig is expected to detect all investigated erosion severities within ± 0.2 axial chord lengths around the rotor leading edge under transonic conditions.

Keywords: Axial turbomachinery, Compressor blades, Leading-edge erosion, In-situ damage detection, Aerodynamic performance, Sensor detectability limits.

Acknowledgements

I would like to express my sincere gratitude to my supervisors, Marcus Lejon and Hans Mårtensson, for their guidance and support throughout this thesis. I am also grateful to the entire DARLING NFFP project team for their insightful contributions and engaging discussions along the way.

A special thanks to my colleagues and fellow master's thesis students at GKN Aerospace for their assistance and for making my time at GKN both productive and enjoyable.

I would also like to thank my examiner, Niklas Andersson, for his constructive feedback and academic support during this work.

Finally, I would like to thank my partner, Lisa Josefsson, for her unwavering support, as well as my family and friends for their encouragement throughout this journey.

Alexander Boström, Gothenburg, June 2025

List of Acronyms

Below is the list of acronyms that have been used throughout this thesis:

ISA	International Standard Atmosphere
RANS	Reynolds-Averaged Navier–Stokes
SST	Shear Stress Transport
REFP	Reference Point
NSP	Near-stall Point
FFT	Fast Fourier Transform
BPF	Blade Passing Frequency
CFD	Computational Fluid Dynamics

Nomenclature

Below is the nomenclature of parameters and subscripts that have been used throughout this thesis.

Parameters

T_0	Total temperature [K]
p_0	Total pressure [Pa]
ρ	Density [kg/m^3]
a	Speed of sound [m/s]
M	Mach number
C_p	Static pressure coefficient
s	Entropy
η_p	Polytropic efficiency
$\dot{m}$	Mass flow rate [kg/s]
ϕ	Flow coefficient
ψ	Stage loading coefficient
V_x	Axial velocity component [m/s]
U	Blade speed [m/s]
V_w	Tangential component of absolute velocity [m/s]
V, V_r	Absolute and relative velocity vectors [m/s]
α	Swirl angle [rad or deg]
β	Relative swirl angle [rad or deg]
y^+	Dimensionless wall distance
ΔS	Entropy rise

Subscripts

1, 2	Inlet (1) and outlet (2) flow stations
∞	Far-field reference condition

Contents

List of Figures

List of Tables

1
Introduction

1.1 Background

Over the past decade, significant advancements have been made in axial turbomachinery technology, particularly in enhancing efficiency and reducing operational costs in aviation applications [1]. These machines comprise of numerous critical components that directly contribute to the overall performance and economic feasibility of the machine, with the compressor system being one of the most vital modules. Extensive research has been conducted to improve various aspects of compressor systems, both in their development and operational lifespan.

This study will focus on the latter—specifically, the in-situ automatic detection of damage and wear in compressor blades, with the potential to enhance operational efficiency, reliability, and safety throughout their service life. Here, "in-situ" refers to detecting damage directly within the compressor's operational environment, without requiring disassembly or interrupting its function. This capability could pave the way for intelligent repair and maintenance strategies in the future.

The work presented in this thesis was conducted within the framework of the Darling NFFP project [16], a collaborative research initiative involving GKN Aerospace, KTH – Energiteknik, and the University of Stuttgart's Institut für Thermische Strömungsmaschinen (ITSM). The thesis itself was carried out at GKN Aerospace.

1.2 Purpose and Goals

The purpose of this thesis is to investigate the aerodynamic effects of leading-edge erosion on a compressor rotor blade, operating under both subsonic and transonic flow conditions. The study focuses on understanding how increasing erosion severity alters both local flow phenomena—such as shock structures, separation bubbles, and tip-leakage vortices—and global performance metrics, including efficiency and loss generation.

A key objective is to determine the measurable limits of such erosion effects using the current instrumentation available at a specific experimental test rig. This involves identifying the minimum severity of leading-edge damage that produces a detectable change in the static pressure field and spectral content of the sensor signals. The work includes a detailed numerical analysis of the flow field and its

evolution with erosion, under multiple operating points.

The findings of this study aim to support future experimental efforts by:

- Guiding the selection of appropriate erosion geometries for manufacturing a synthetically eroded rotor blisk.
- Informing the optimal placement and resolution requirements of pressure sensors for erosion monitoring.
- Assessing whether the current sensor configuration at a specific experimental rig is sufficient to detect early-stage erosion effects.

Overall, the thesis combines aerodynamic performance evaluation with measurement feasibility analysis to establish a comprehensive framework for erosion detection and instrumentation planning in axial compressors.

2
Theory

2.1 Axial compressor

An axial compressor is well suited for applications requiring a large pressure rise of the working fluid while maintaining a high flow rate. A compressor typically consists of multiple stages, each comprising a rotor followed by a stator. In jet engines, the pressure increase is achieved through a multistage compressor, which is coupled via a shaft to a turbine located further downstream. The turbine provides the necessary power to rotate the compressor's rotor blades.

The pressure rise in an axial compressor is achieved by allowing gas to enter at a large radius and compressing it through the interaction between the rotors and stators. As the gas becomes denser, the flow area is usually reduced from one stage to the next in order to maintain a relatively constant axial velocity. If the flow is drawn directly from the atmosphere, the first compressor stage is often preceded by a set of inlet guide vanes, positioned upstream to enhance the operational range.

2.1.1 Velocity Triangle

Figure 2.1 illustrates the velocity triangles at the rotor inlet and outlet of an axial compressor stage. These triangles describe the vector relationship between the absolute velocity $\mathbf{V}$, the rotor blade speed $\mathbf{U}$, and the relative velocity $\mathbf{V}_r$. Each triangle also defines the key flow angles:

$\alpha =$ Angle between $\mathbf{V}$ and the axial direction (swirl angle)
$\beta =$ Angle between $\mathbf{V}_r$ and the axial direction (relative swirl angle)

Inlet Triangle: At the rotor inlet (station 1), the absolute velocity $\mathbf{V}_1$ can be decomposed into an axial component V_{f1} and a tangential component V_{w1}, assuming that the radial velocity is zero:

$$\mathbf{V}_1 = V_{f1} + V_{w1}$$

The flow enters the rotor at an swirl angle α_1. The rotor blade moves with tangential speed U, so in the rotating frame, the fluid velocity relative to the blade is:

$$\mathbf{V}_{r1} = \mathbf{V}_1 - \mathbf{U}$$

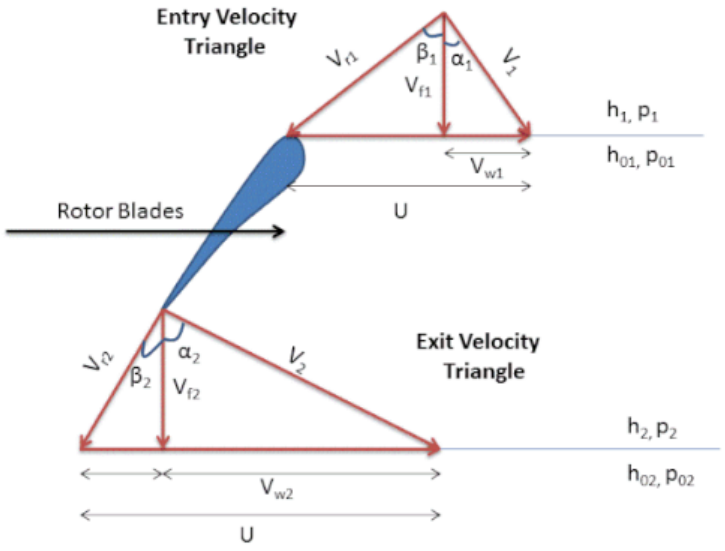

Figure 2.1: Velocity triangles at the rotor inlet (top) and outlet (bottom), showing absolute, relative, and blade velocities. Image adapted from [20].

Outlet Triangle: At the rotor outlet (station 2), the same relations apply. The absolute velocity $\mathbf{V}_2$ has an associated swirl angle α_2, and the relative velocity $\mathbf{V}_{r2} = \mathbf{V}_2 - \mathbf{U}$ defines the relative swirl angle β_2. The change in the absolute tangential velocity across the rotor,

$$\Delta V_w = V_{w2} - V_{w1}$$

2.1.2 Work Done by the Rotor

Applying the velocity triangles at the rotor inlet and outlet, the specific work done by the rotor on the fluid is governed by the change in the tangential component of the absolute velocity. This is expressed by Euler's turbomachinery equation:

$$w = h_{02} - h_{01} = U \cdot V_x \cdot (\tan \alpha_2 - \tan \alpha_1) = U \cdot V_x \cdot (\tan \beta_2 - \tan \beta_1) \tag{2.1}$$

For axial inflow conditions, the axial velocity V_x is typically equal to the inlet axial component $V_{f1} = V_{f2}$. This relation links blade geometry (through α or β) to the stage work input and forms the foundation for aerodynamic design and analysis in axial compressors.

2.1.3 Total Pressure and Total Temperature

To accurately compute the total-to-total ratio across a rotor, it is essential to evaluate the total (stagnation) pressures or temperature at specific stations within the compressor. The total pressure at a point in the flow is the pressure the fluid would

attain if it were isentropically brought to rest.

Referring to Figure 2.1, the total pressure at station 1 is computed from the static pressure and Mach number using the isentropic relation:

$$P_{01} = P\left(1 + \frac{\gamma - 1}{2} M_1^2\right)^{\frac{\gamma}{\gamma - 1}} \tag{2.2}$$

where:

- P_{01} is the total pressure at station 1,
- P is the static pressure,
- $M_1 = \frac{V_1}{c_1}$ is the Mach number,
- V_1 and c_1 represent the absolute velocity and the speed of sound, respectively.
- γ is the ratio of specific heats

The total temperature T_0 at the same station is calculated using:

$$T_{01} = T\left(1 + \frac{\gamma - 1}{2} M_1^2\right) \tag{2.3}$$

where T is the static temperature.

$$\mathrm{PR}_{\mathrm{tt}} = \frac{P_{02}}{P_{01}} \tag{2.4}$$

$$\mathrm{TR}_{\mathrm{tt}} = \frac{T_{02}}{T_{01}} \tag{2.5}$$

These ratios are key metrics for assessing the performance achieved by a stage in an axial compressor.

2.1.4 Flow and Stage Loading Coefficient

Two important non-dimensional parameters in axial turbomachinery are the flow coefficient and the stage loading coefficient. These coefficients characterize the aerodynamic behavior of the stage and are especially useful in design and performance analysis.

Flow Coefficient (ϕ): The flow coefficient is defined as the ratio of the axial velocity to the blade speed:

$$\phi = \frac{V_x}{U} \tag{2.6}$$

where:

- V_x is the axial component of the absolute velocity,
- U is the rotor blade speed.

Stage Loading Coefficient (ψ) : The stage loading coefficient reflects the aerodynamic loading of the stage and is defined by the inlet and outlet flow angles:

$$\psi = 1 - \phi(\tan\alpha_1 - \tan\beta_2) \tag{2.7}$$

where:

- α_1 is the swirl angle at rotor inlet,
- β_2 is the relative swirl angle at rotor outlet.

Together, the flow coefficient ϕ and the stage loading coefficient ψ describe the relationship between geometry, flow turning, and energy transfer within the stage. They are also central in constructing compressor performance maps and comparing different designs.

2.1.5 Pressure coefficient

Pressure variations over the rotor blade surface are analyzed using the static pressure coefficient C_p, as defined in Equation (2.8), where P_∞ is the upstream far-field static pressure, and when used in this report, stagnation pressure,$P_{0,\infty,\text{rel}}$ is the stagnation pressure in the rotor's rotating frame of reference.

$$C_p = \frac{P_s - P_\infty}{P_{0,\infty,\text{rel}} - P_\infty} \tag{2.8}$$

2.1.6 Compressor Map Performance

When operating a compressor under conditions outside its design point, the compressor can be susceptible to either stalling or choking. If the flow coefficient is larger than its design value, the increase in flow rate causes a decrease in the blade loading coefficient, which can lead to choking the flow. Similarly, if the flow coefficient decreases, the blade loading increases, ultimately leading to stall, as demonstrated in Figure 2.2.

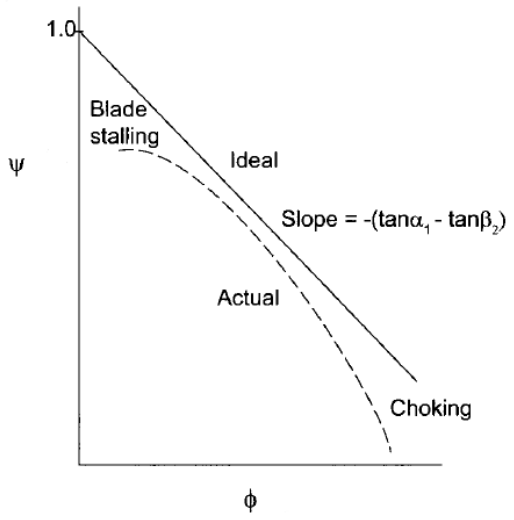

Figure 2.2: Performance characteristics of a compressor stage.

Equations 2.6 and 2.7 provides the ideal compressor characteristics plotted in Figure 2.2, as well as some typical real compressor characteristics. Any deviations from the

ideal line are caused by irreversibilities.

In order to characterize the performance of a compressor, the total pressure ratio is plotted as a function of the flow rate, with efficiency curves superimposed on a set of curves obtained for constant rotational speed, also known as speedlines. Here, the flow rate are modified to a corrected mass flow rate, as illustrated in Figure 2.3.

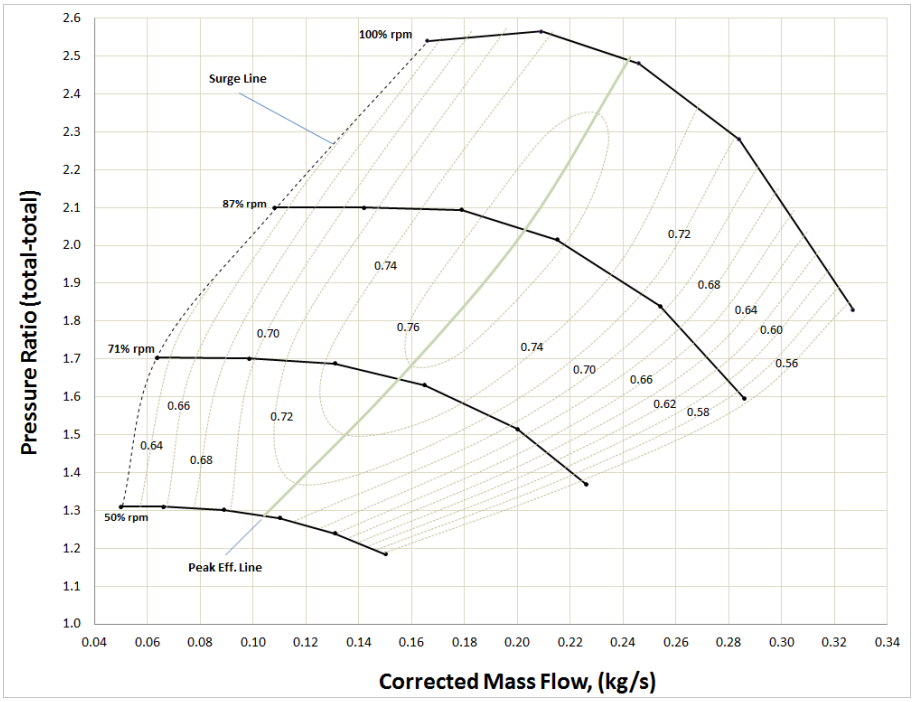

Figure 2.3: Performance characteristics of a compressor. Figure from [21]

As seen in the figure, each speedline terminates at a boundary known as the surge line. If the flow rate decreases beyond this line, the rotor blades in the compressor will stall. A severe stall can lead to a condition known as surge, where the flow may reverse direction, potentially causing severe damage to the engine.

On the other hand, at high flow rates follwing a constant speedline in the figure, the flow in the blade passages will choke, which is indicated by the sharp drop of the curvature of that line. Chocking occurs when the flow reaches sonic conditions (Mach 1) in the blade passage, beyond which no further increase in mass flow rate is possible without changing the flow conditions upstream.

2.1.7 Compressor Losses

Losses in the compressor arise from multiple sources of flow phenomena and can be categorized into profile losses, secondary flow losses, and losses in the annulus boundary layers. Profile losses originate from the growth of the boundary layers along the blades. In literature, secondary flow and annulus boundary layer losses are typically grouped together, as it is difficult to separate them from each other.

The physical cause of secondary flow is the curvature along the flow path. An example of secondary flow in a compressor occurs due to the interaction between one or both endwall boundary layers and the blade. These endwall locations are typically referred to as the hub or shroud, as illustrated in Figure 2.4.

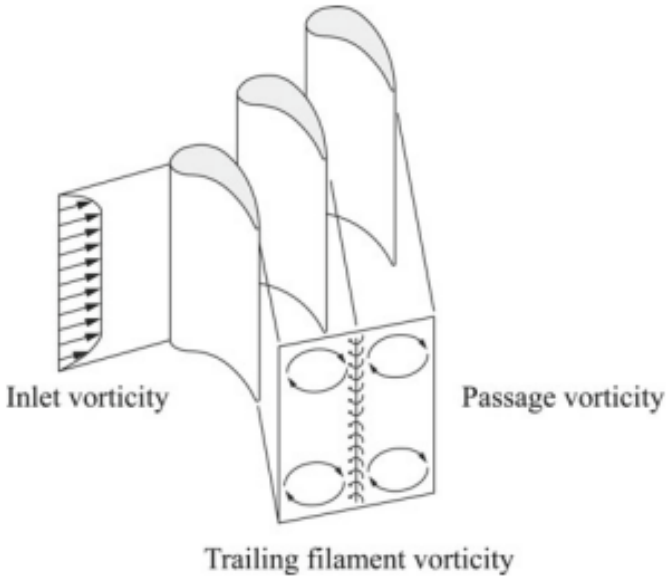

Figure 2.4: Endwall secondary flow in a compressor. Figure from [23]

Within the endwall boundary layer, viscous forces slow down the flow near the surface. As a result, an unbalanced pressure force induces transverse flow along the endwall boundaries, directed toward the suction side of the blade.

In the stator section of a compressor, this results in the formation of two counter-rotating secondary vortices, originating from the boundary surfaces of both the hub and shroud. These vortices have their rotational axes aligned with the main flow direction, leading to induced secondary flow.

In contrast, for a rotor section, typically only one counter-rotating secondary vortex forms at the endwall, the hub. Also, another significant source of secondary flow arises from tip leakage, which occurs due to a clearance gap between the rotor blade tip and the shroud. This gap allows high-pressure air to leak from the pressure side to the suction side of the blade.

As this leakage flow traverses the passage, it rolls up into a vortex, forming the tip leakage vortex. This vortex migrates across the passage, further interacting with the secondary vortices generated at the endwall. The complex interaction between tip leakage flow and endwall secondary flow significantly influences the overall aerodynamics of the compressor stage. A tip leakage vortex is illustrated in Figure 2.5.

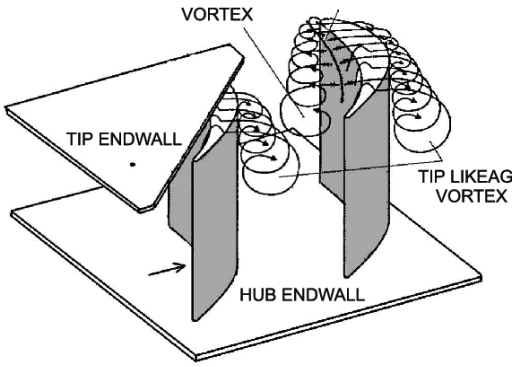

Figure 2.5: Tip leakage vortex in a compressor. Figure from [24]

2.1.8 Compressor Efficiency

When defining the efficiency of a compressor stage, the concept of polytropic efficiency is often used [2]. The use of polytropic efficiency is based on the fact that the increase in temperature due to irreversible friction in one stage results in additional work being required in subsequent stages—this effect is known as the preheat effect.

Polytropic efficiency, also referred to as small-stage efficiency, is defined as the isentropic efficiency of an infinitesimally small (differential) stage, such that it remains constant throughout the entire compression or expansion process.

For analyzing the fluid dynamics of individual stages in either compressors or turbines, polytropic efficiency provides a more accurate representation of real thermodynamic processes than isentropic efficiency, as it accounts for small incremental changes in pressure and temperature, leading to a more reasonable basis for comparison [3].The polytropic efficiency is defines as:

$$\eta_p = \log\left\{\left(\frac{P_{03}}{P_{01}}\right)^{\frac{\gamma-1}{\gamma}}\right\} \Big/ \log\left(\frac{T_{03}}{T_{01}}\right) \tag{2.9}$$

where:

- T_{03}, T_{01} are the stagnation temperatures in the absolute frame of reference at the compressor exit and inlet, respectively.
- P_{03}, P_{01} are the stagnation pressures in the absolute frame of reference at the compressor exit and inlet, respectively.

2.2 Pressure transducer

A pressure transducer generates an electrical output proportional to the applied pressure. When pressure is exerted, it introduces a force on a sensing element within the sensor, causing mechanical deformation. This deformation alters the electrical characteristics of the sensing element, resulting in a corresponding change in the transducer's output signal. Pressure transducers are available with four types of reference pressure configurations: (a) **Absolute** (psia), (b) **Gauge**, (c) **Differential**,

and (d) **Sealed Reference**, as illustrated in Figure 2.6.

In high-fidelity aerodynamic or turbomachinery applications, transducers must exhibit high linearity, fast frequency response, and thermal stability. The usable frequency range is typically limited by the transducer's natural resonance frequency. To ensure accurate and undistorted measurements, the frequency content of the pressure signal should remain below approximately one-fifth of this resonance frequency, where the transducer exhibits a flat frequency response [22].

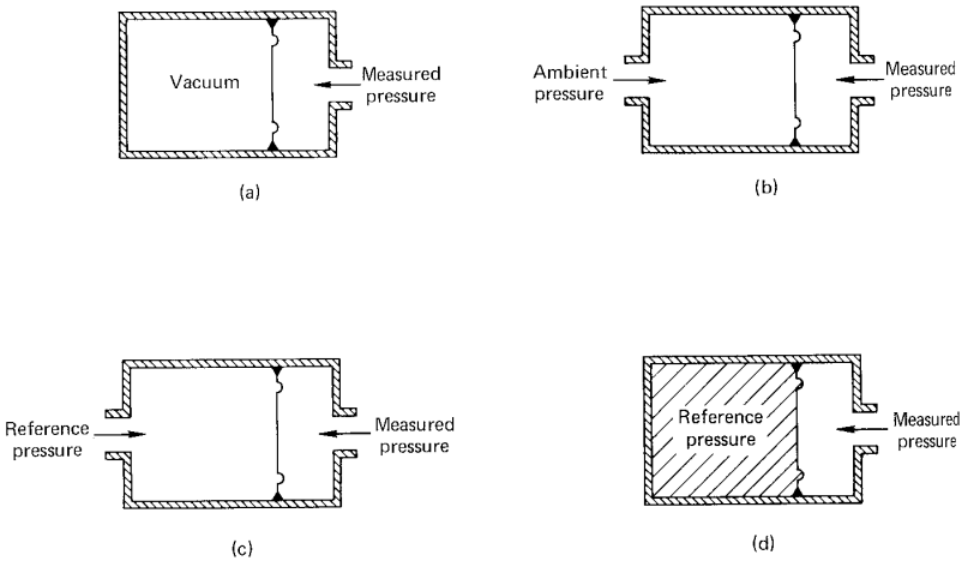

Figure 2.6: Pressure transducer reference types. Figure from [22].

2.3 Fast Fourier Transform (FFT)

When analyzing a discrete signal, such as the static pressure from a sensor, it is often useful to transform the signal from its original time domain to the frequency domain to analyze its fluid dynamics and/or acoustic characteristics. This transformation is done using the Discrete Fourier Transform (DFT) on a sequence of measurement samples in time. The DFT of an N-point sequence $x[n]$ is defined as:

$$X[k] = \sum_{n=0}^{N-1} x[n] e^{-j\frac{2\pi}{N}kn} \tag{2.10}$$

where $X[k]$ represents the frequency spectrum of the signal, $x[n]$ is the time-domain signal, N is the number of points in the sequence, and k is the frequency index.

The FFT algorithm significantly reduces the computational complexity of the DFT from $O(N^2)$ to $O(N \log N)$ by exploiting symmetries in the DFT matrix. This efficiency makes FFT suitable for real-time signal processing and large datasets.

3
Previous work

3.1 Mechanisms of Compressor Blade Degradation

Compressor blade performance degradation occurs through three primary mechanisms: **fouling**, **clearance increase**, and **operational wear** [5].

- **Fouling** involves the accumulation of particles, such as industrial pollutants, on the blade surfaces, leading to performance losses. In the aviation industry, this type of degradation is typically managed through periodic engine washing during maintenance intervals.
- **Clearance increases** are mainly caused by thermal transients leading to casing ovalization, and changes in rotor bearing stiffness. Uneven thermal expansion between components can result in rubbing. If bearing adjustments are insufficient, these effects can combine and cause significant clearance growth, particularly in the mid and rear sections of the compressor.
- **Operational wear** results from prolonged exposure to airborne particles like sand and water, encountered in operational environments of a aircraft engine, and frequent online washing. This leads to an erosion process that gradually alters the blade's shape.

3.2 Erosion Morphology and Modeling Approaches

The process of erosion results from the frequent impact of particles in a flow over a material. This impact leads to the abrasive removal of material from the surface in contact. Hamed [6] experimentally showed that the highest erosion rate in a turbomachine occurs in the first stage of the compressor, namely at the rotor blade leading-edge. As particles collide with the rotor blade, they are centrifuged in the radial direction, substantially accumulating the highest erosion rate at the tip of the leading edge. Hamed concluded that, in compressors, first-stage rotor erosion causes reduced chord length, leading-edge tip corner rounding, and thinning. Further research [7] has shown that the formation of an eroded leading edge is typically caused by particles with diameters of 20 μm or more. This erosion increases surface roughness and alters the overall surface profile. Consequently, it modifies the leading edge shape, affecting the incidence angle, changes the airfoil throat opening, and increases both blade tip and seal clearance.

Rotor blade leading-edges are typically designed with regular geometries, such as circular or elliptical shapes, that can be mathematically defined. However, erosion creates irregular morphologies that degrade performance through complex mechanisms. Studying these erosion patterns is challenging due to the small size of the leading-edge radius, which, despite the relatively large overall rotor blade size in turbofan engines, is typically only a few millimeters. Despite these challenges, Ma [8] successfully studied the progressive loss of original material from a blades surface through erosion processes. The study divided the evolution of blade erosion into distinct stages to characterize these morphological changes. Building on Ma's work, Shi [1] further defined these stages into four distinct topological phases: New Blade, Cliff and Canyon, Flat Canyon, and Blunt with Fillet, as illustrated in Figure 3.1.

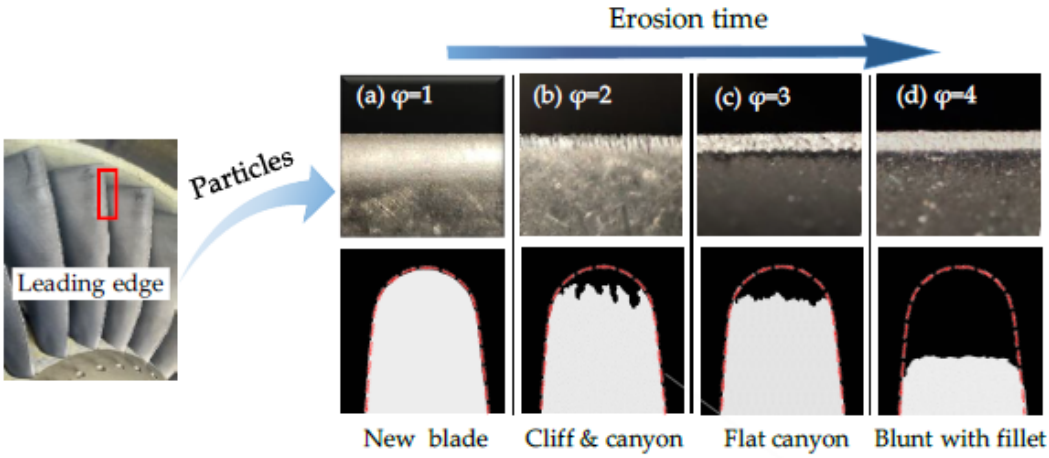

Figure 3.1: Topological phases of blade erosion as defined by Shi. Figure from [1]
.

Shi [1] also reviewed how erosion on the leading-edge is modeled in the literature and concluded that, although the erosion process is complex, directly modeling the erosion of the blade leading edge significantly simplifies the process and facilitates the study of its influence on aerodynamic performance. This simplification is usually achieved by directly cutting the leading edge of the blade to simulate the effects of erosion, with the chord length decreasing linearly along the blade height until no material is removed at the hub. Roberts et al. [9] extended the approach beyond simply cutting the leading edge to create a blunt blade. They optimized the eroded leading-edge shape by rounding it and introducing surface roughness and twisting, making it more representative of the characteristics of a realistically eroded blade, as illustrated in Figure 3.2.

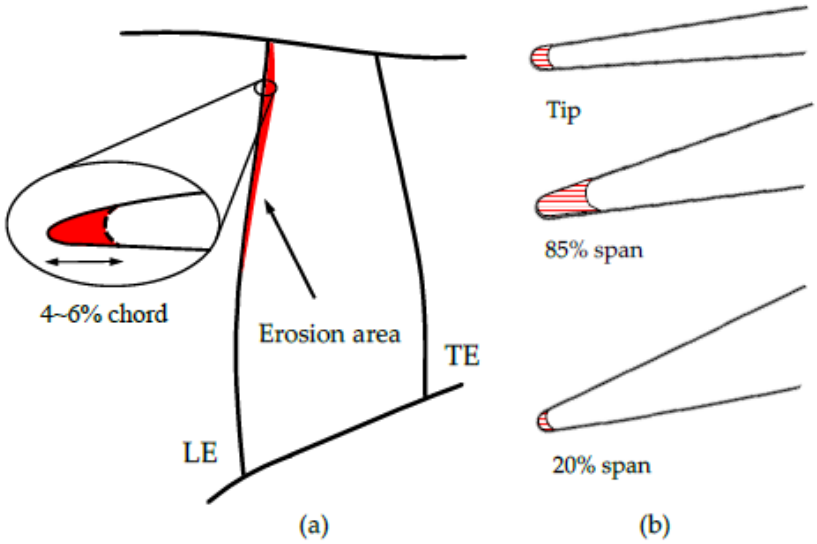

Figure 3.2: Erosion modeling approaches, including simplified cutting and optimized shapes with roughness and twisting, as defined by Roberts et al. [9].

3.3 Effects of leading-edge erosion

Goodhand et al. [15] investigated the effects of leading-edge pressure spikes caused by erosion on profile loss, using the stator of a single-stage low-speed compressor and a range of leading-edge geometries. It was found that if the erosion exceeded a critical height, the leading-edge boundary layer separation would occur closer to the leading edge, causing a premature transition from laminar to turbulent flow and ultimately increasing profile loss up to 30 % at positive incidence angles. Experimental and simulated results from cascades of a one-stage compressor, before and after erosion, as reported by [14], indicate that erosion generally causes a change in the pressure distribution in the compressor stage across a range of increasing mass flows. This reduction was found to be a function of compressor speed and the location of the stage where the erosion occurs. The study also indicates that erosion on a compressor stage causes a reduction in the mass flow rate. It was also found that this reduction in mass flow was connected to an increase in rotational speed. [12] focused on a transonic axial compressor whose blade was damaged due to operation in sandy environments. CFD studies were conducted for a damaged first-stage rotor of the GE T700-401C compressor. It was found that erosion at the leading edge caused significant differences in the flow physics across all blade passages. Compared to a undamaged blade, the study observed a more pronounced shock expansion field, a shift in the bow shock, and a stronger near-normal shock at the suction-side in passage. It was concluded that eroded blades generate significantly larger high-loss regions adjacent to the blade surfaces in passages on either side of the damage. This was attributed to reductions in stagnation pressure and temperature ratios, as well as a decline in adiabatic efficiency. Experiments by [11], in which sand was injected into the flow of an axial compressor, demonstrated a reduction in stage loading and rotor

turning. Similarly, as observed in [12], erosion resulted in significant decreases in stagnation pressure and temperature ratios, primarily due to increased losses at the blade leading edge, especially in the tip region. These findings suggest that leading-edge deterioration and airfoil shape changes were the main contributing factors. The phenomenon of increased tip leakage was investigated by [10], revealing that the interaction between tip leakage and passage flow in an eroded rotor cascade caused vortex breakdown and near-endwall flow collapse. Where tip leakage flow exhibited unsteady behavior, with fluctuations and instability. A non-linear relationship was found between blade tip erosion and the stable operating range.

4

Technical Approach

4.1 Experimental Setup

The compressor stage was evaluated in parallel with this study using the axial experimental compressor facility at the University of Stuttgart. A CAD rendering of the experimental setup is shown in Figure 4.1.

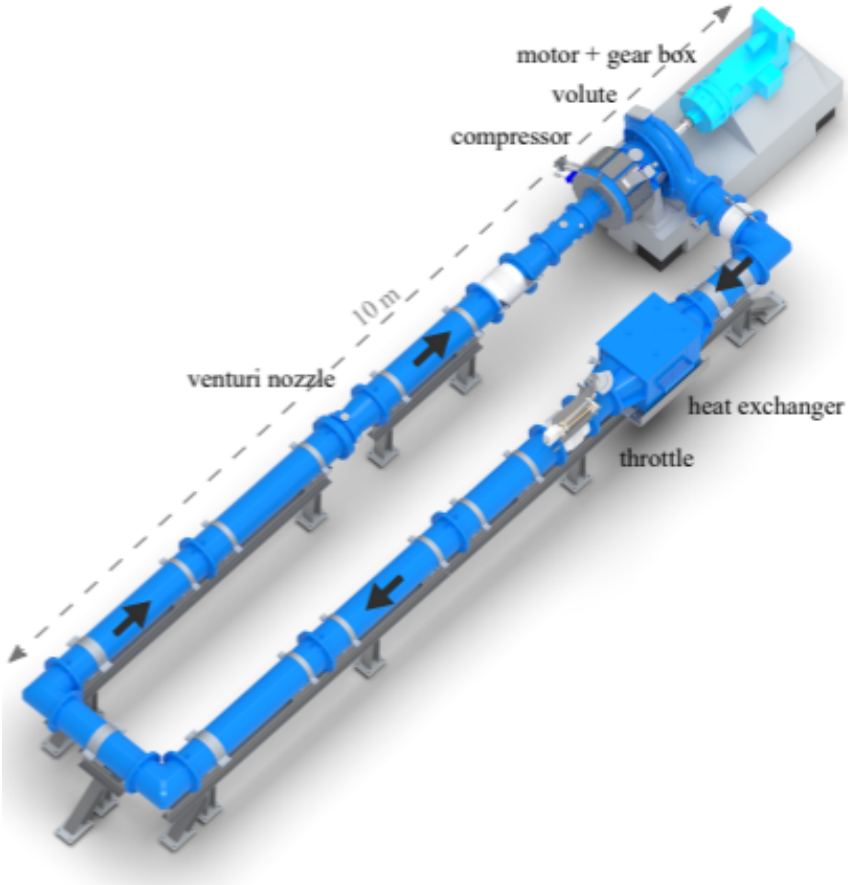

Figure 4.1: CAD rendering of the compressor facility at the University of Stuttgart. Figure from [19].

The gas channel in the rig forms a closed circuit, enabling experiments with various gases, not just air. This flexibility is advantageous for achieving engine-realistic Mach numbers, by lowering the speed of sound in the gas channel. The compressor

stage has been tested using air and is intended to operate with R134a as the working fluid in future testing campaigns. Instrumentation is provided to measure flow quantities relevant to assessing compressor performance. Rapid pressure sensors (Kulites) are installed in the outer casing to detect high-frequency flow variations in the static pressure field. Additionally, probes are installed to measure static and total pressure averaging, while other sensors include total temperature probes and a blade tip timing system. A complete description of the sensor arrangement at the facility is shown in Figure 4.2.

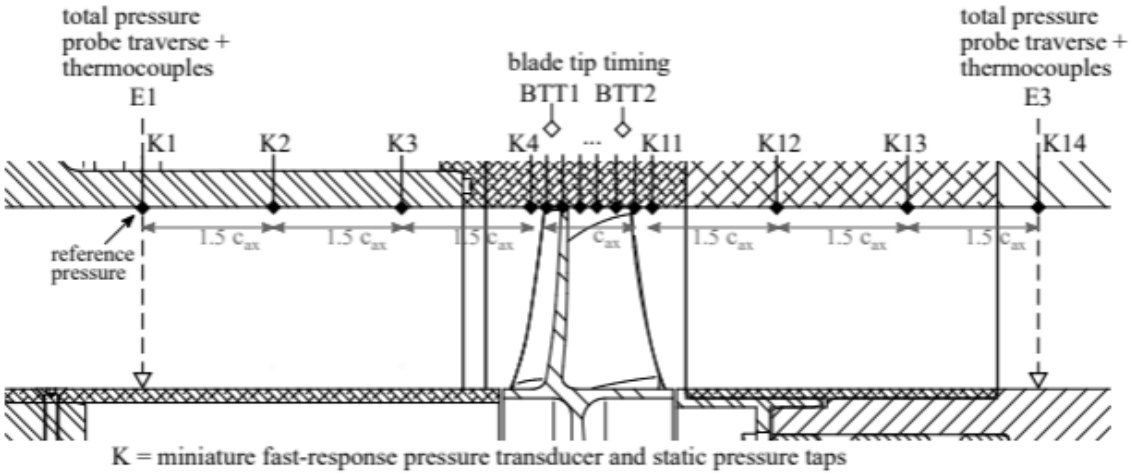

Figure 4.2: Meridional cut of test section showing sensor positions from Ref. [19].

4.2 Geometry

The subject of this study is a transonic single-stage research compressor rotor assembly. The rotor disk geometry JULIA was collaboratively designed for the Stuttgart rig in the NFFP CoFAS project. CoFAS is an acronym for "Compressor and Fan Aeroelasticity and Stability limits". The project was funded by the Swedish Aeronautical Research Program. The relevant performance data is listed in Table 4.1. In this study, a simplified geometry was investigated, featuring only the rotor blisk. Figure 4.5 presents several views of a single passage of the first-stage rotor blisk geometry. The study was conducted with a tip clearance of 0.2 [mm] between the blade tip and the shroud casing. To evaluate the impact of changes in rotor performance, measurements were taken from stations located upstream and downstream, close to the rotor's leading and trailing edges, as illustrated in Figure 4.6.

Table 1	Design data for JULIA
Diameter	240 mm
Design mass flow	3.68 kg/s
Design pressure ratio	1.64
Design shaft speed (100%)	17,105 rpm
No. of rotor blades	18
Rotor aspect ratio	2.18

Table 4.1: Design data for JULIA.

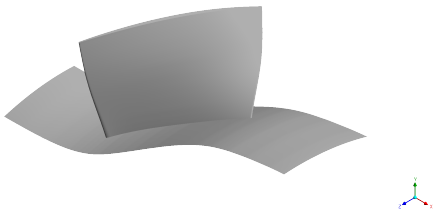

Figure 4.3: Isometric view of the rotor blade geometry.

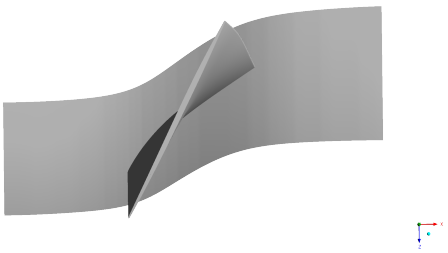

Figure 4.4: Top view of the rotor blade geometry.

Figure 4.5: Various views of the first-stage rotor blade geometry.

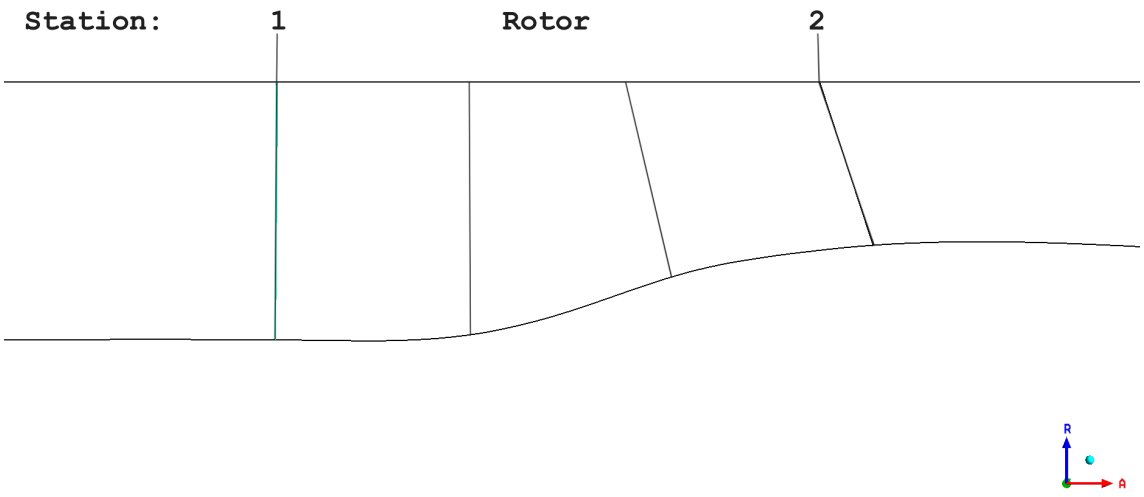

Figure 4.6: Simplified blade passage with radial measurement stations.

4.3 Numerical Settings

The CFD calculations in this investigation were performed at steady state, using the Reynolds-Averaged Navier-Stokes (RANS) equations. Menter's Shear Stress Transport (SST) model was applied as the turbulence model. For calculations using R134a as the working fluid, the reattachment modification was enabled. Boundary layer transition was not modeled, and the flow was considered fully turbulent at the inlet boundary. All cases were run using the ANSYS High Resolution scheme [17] with double precision. The blade and endwall surfaces were defined as adiabatic, non-slip, and rotating walls. The blade and hub geometry were set to rotate, while the shroud was set to counter-rotate. Rotationally periodic boundaries were applied to the sides. Depending on the working gas that was used in the investigation, the inlet boundary conditions were set to either constant or a profile value of total pressure, total temperature and flow direction (Axial, Radial and Theta component). While the outlet boundary condition was set to a constant of average static pressure. The specific boundary conditions are presented in the subsequent method section of chapter 5 (Air) or chapter 6 (R134a).

4.4 Computational Domain and Mesh

A computational domain was established using a single rotating frame approach. Turbogrid was utilized to create a resolved boundary layer mesh, achieving an area average y+ of less than 1. The mesh employed an OH-grid structured configuration with a leading edge mesh refinement. To evaluate the dependence of mesh resolution on performance parameters, both global performance metrics and local differences at the shroud were investigated. For the global performance metrics, mesh studies were conducted for all operational points of analysis, using a nominal blade geometry.

In terms of measurable limits, grid independence in local areas along the shroud is of particular interest in this study. Selecting an adequate grid size is essential to capture small variations in flow quantities at shroud locations, especially when introducing small increments in rotor leading edge erosion. To confirm this, the local difference at the shroud in static pressure around the circumferential at an axial point near the leading edge was examined between increasing mesh sizes for an eroded geometry.

Tip clearance is a critical factor in this study. It is essential to ensure that the mesh resolution is fine enough to accurately capture the flow characteristics in the tip clearance region. This includes the ability to resolve the boundary layer and any potential flow separation or recirculation that may occur. The tip clearance was carefully modeled to reflect realistic operational conditions, and the mesh was specifically refined in this area with increasing mesh size to ensure sufficient fidelity in the simulation results.

The mesh sizes for a single-blade passage is presented in Table 4.2. The same

grid is used for both air and R134a gas cases, as well as for nominal and eroded geometries. Views of a fine mesh are shown in Figures 4.7 and 4.8.

Mesh	**Cells**	**Cell Offset to Wall [mm]**	**Cells Shroud - Tip**
Very Coarse	587 783	0.004	15
Coarse	1 102 060	0.002	18
Medium	2 175 168	0.001	21
Fine	4 179 600	0.001	24
Very Fine	8 031 200	0.001	27
Extremely Fine	15 570 956	0.001	30

Table 4.2: Mesh Study Details.

Figure 4.7: Fine computational grid.

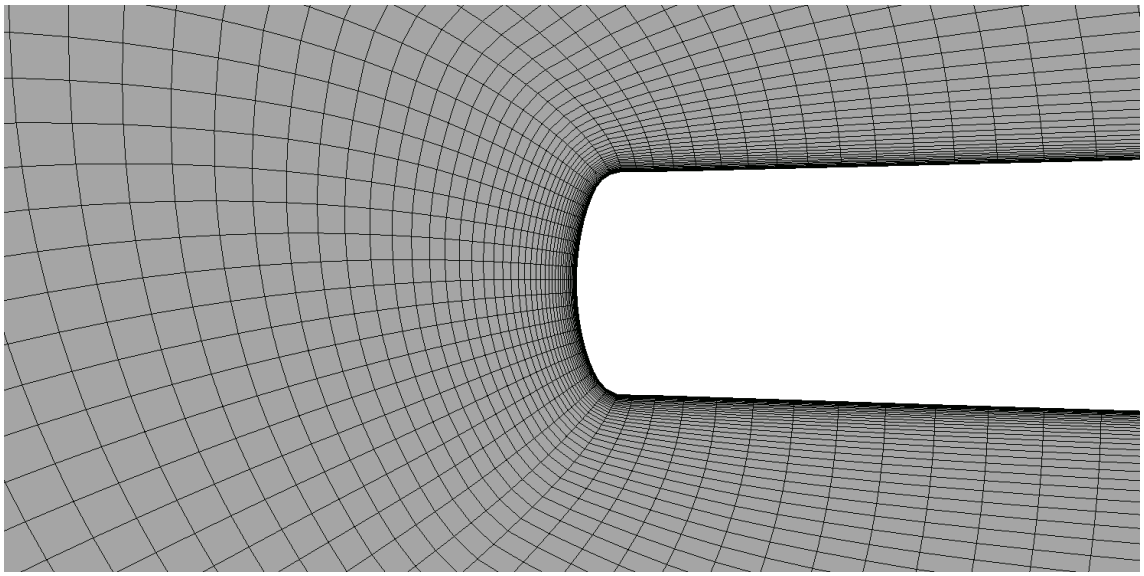

Figure 4.8: Local mesh refinement at the blade leading-edge at 90 % span for a fine mesh.

To capture the static pressure distribution along the shroud, pressure probes were placed at multiple axial locations within the computational domain, replicating the sensor positions used at the Stuttgart University experimental rig. An overview of the probe locations in the computational setup is provided in Figure 4.9.

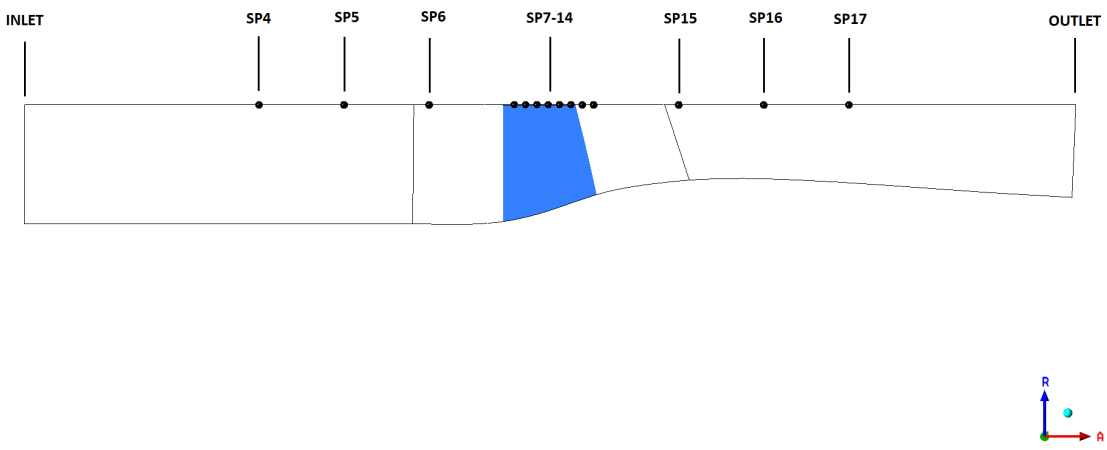

Figure 4.9: Computational domain with sensor positions.

4.5 Erosion Methodology

Several cases of erosion severity were simulated during this study using a consistent erosion methodology, in conjunction with the investigation carried out by Ma et al. [8]. In this study, erosion is considered a geometrical deviation from the nominal blade geometry, characterized by changes in the leading-edge radius resulting in a more blunt profile compared to the nominal elliptical shape, and a decrease in blade chord length. The change in chord length reduction was modeled to increased linearly from the hub to the blade tip, with the maximum leading edge radius and chord reduction at occurring at the tip.

Figures 4.10 show airfoil sections of the compressor rotor blade with the nominal geometry compared to a representative eroded blade, featuring a blunt leading edge shape and a linear reduction in chord length from 10 % to 90 % span.

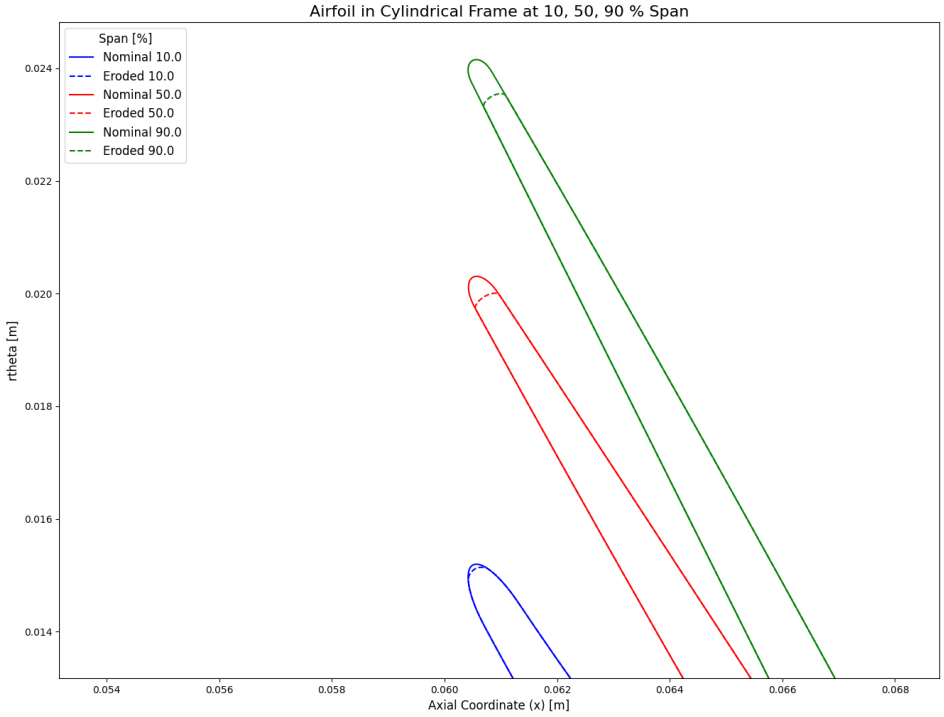

Figure 4.10: Comparison of nominal and eroded blades at 10, 50, 90 % span.

4.6 Target Operational Conditions

In this study, two different operational points were investigated. One is referred to as the reference point, or REFP in the text. This point was intended to be close to what would be considered a design point for the rotor blade. The other point was

intended to represent an operational point close to where the flow would start to separate from the blade surfaces, causing compressor stall. In the text, this point is called near-stall, or NSP.

In order to determine the average static outlet pressure condition for the two operational points of interest, a speedline was simulated for each test case (air and R134a) at a constant rotational speed of $17,000$ and $17,105$ RPM respectively, where the average pressure at the outlet was increased until the rotor approached the surge line.

4.7 Verification and Validation

The full rotor setup was tested with air as the working fluid in the experimental compressor rig. At the time of this investigation, R134a had not yet been tested. The case-specific operating conditions applicable to this study are compared in the subsequent results chapter for validation purposes.

5
Subsonic Flow (Air)

This chapter investigates the aerodynamic impact of leading-edge erosion under subsonic flow conditions, serving as a baseline to isolate erosion effect from compressibility-dominated phenomena (e.g., shocks). Additionally, the investigation setup will only consider the rotor effects on the flow field. Any other geometrical effects, such as inlet guide vanes or downstream stators, are excluded from this part, which is consistent with the scope of previous investigations conducted in the experimental rig. The nominal blisk is compared to increasing erosion severity, investigating fundamental degradation mechanism such as boundary layer growth, separation and operational point shifts - that underpin potential performance losses. These insights contributes to the context of analysis in Chapter 5, where compressibility effects is added to the context of leading edge erosion.

5.1 Method

This section outlines the methodology used to evaluate the aerodynamic impact of erosion on a subsonic compressor rotor. The approach includes a systematic variation of erosion severity, standardized inlet and outlet boundary conditions, and mesh sensitivity analysis to ensure numerical accuracy. The methodology aims to replicate realistic test conditions and provide a robust foundation for analyzing erosion-induced performance changes.

5.1.1 Erosion

A test series of increasing erosion severity will be investigated in this chapter, with increasing chord reduction from 0.2 to 1.5% at the tip of the rotor. The test cases are divided into four geometrical deviations, with a doubling of severity for each subsequent case. The overall geometrical deviations for each test case at different spans are shown in Figure 5.1.

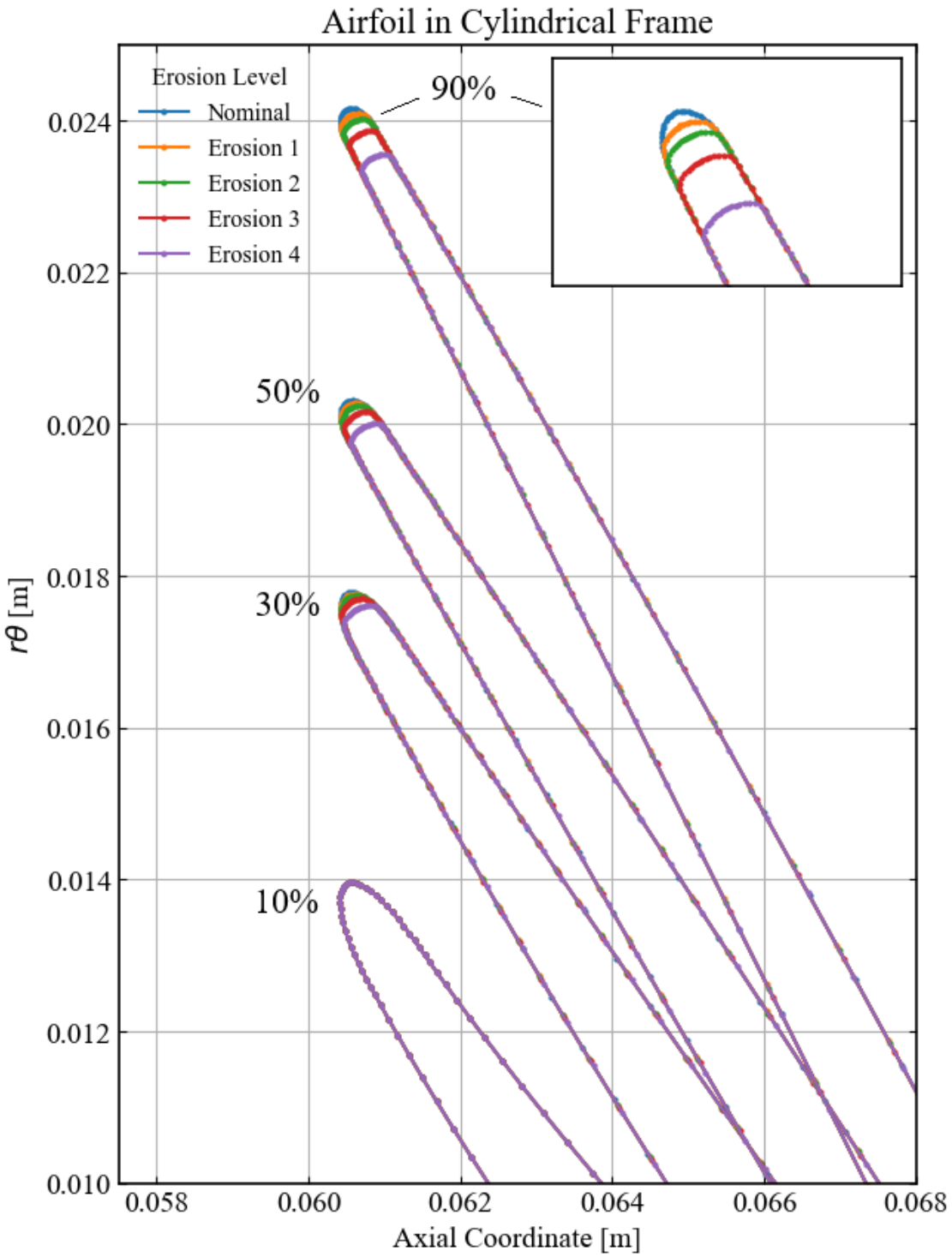

Figure 5.1: Comparison of nominal and eroded blades at different spans (%).

5.1.2 Inlet conditions

In this chapter, the International Standard Atmosphere (ISA) sea-level values for constant total pressure and total temperature was used as inlet boundary conditions. Additionally, the flow is assumed to be fully turbulent throughout the computational

domain. The ISA values for sea-level conditions, as outlined in [18], are summarized in Table 5.1.

Table 5.1: ISA Standard Values at Sea Level

Parameter	Symbol	Value
Total Temperature	T_0	288.15 K
Total Pressure	p_0	101325 Pa
Air Density	ρ	1.225 kg/m^3
Speed of Sound	a	340.29 m/s

5.1.3 Operational Points and Outlet condition

The compressor performance were evaluated through the total and static pressure rise at constant rotational speed to define the outlet boundary condition of constant average static pressure, and to compare the calculated result to experimental data.

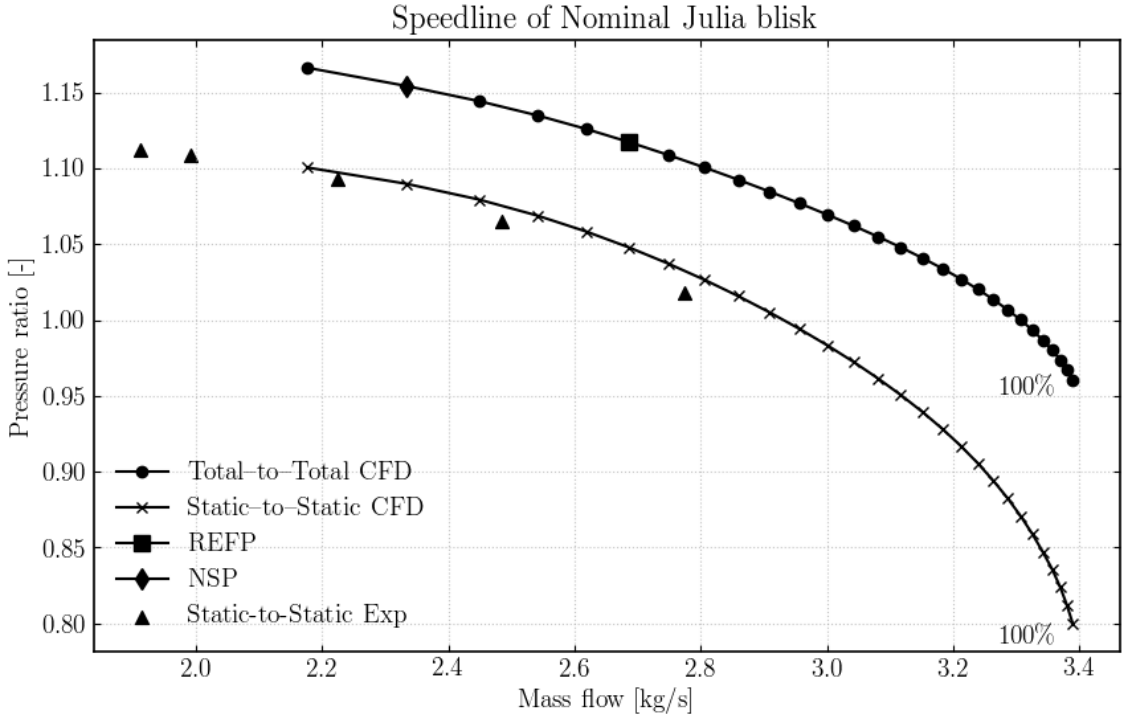

Figure 5.2: Selected operational points (REFP and NSP) and experimental comparison.

From the total pressure curve (Total-to-Total), in Figure 5.2, two operationally points were selected for detailed analysis: Reference point (REFP) and near-stall point (NSP), the values of mass flow and outlet static pressure for these points is found in Table 5.2.

Table 5.2: Mass flow and average static back pressure at selected operational points

Operational Point	**Mass Flow (kg/s)**	**Static Outlet Pressure (kPa)**
Reference Point (REFP)	2.75	101
Near-Stall Point (NSP)	2.33	106

These outlet pressure values were maintained constant across all test cases, i.e nominal and eroded to ensure consistent comparison.

Additionally, in Figure 5.2, the static pressure curve (Static-to-Static) show good agreement with obtained experimental data (triangle markers) from the rig at Stuttgart University, particularly in the region where to two operational points were selected. This experimental correlation confirms that the selected operational points provide physically representative conditions for investigating erosion effects.

5.1.4 Mesh Study

The performance parameters for increasing mesh sizes for the reference point (REFP) and near-stall point (NSP) are shown in Table 5.3 and in Table 5.4 respectively, and Figure 5.3 show the convergence of these parameters, normalized with the results for the finest mesh.

Table 5.3: Mesh Study Results REFP.

Mesh Size	$\mathbf{T}_{static}$ **Ratio**	$\mathbf{P}_0$ **Ratio**	η_p	$\dot{m}$
Very Coarse	1.036926	1.1103	0.911866	2.7289
Coarse	1.036806	1.11034	0.913005	2.73038
Medium	1.036755	1.11047	0.913644	2.72952
Fine	1.036685	1.11059	0.914851	2.73044
Very Fine	1.036592	1.11065	0.915746	2.73116
Extremely Fine	1.036505	1.11061	0.916128	2.73152

Table 5.4: Mesh Study Results NSP.

Mesh Size	$\mathbf{T}_{static}$ **Ratio**	$\mathbf{P}_0$ **Ratio**	η_p	$\dot{m}$
Very Coarse	1.06077	1.15363	0.909045	2.34467
Coarse	1.059609	1.1538	0.909324	2.34358
Medium	1.059126	1.15409	0.909233	2.34011
Fine	1.058764	1.15433	0.909992	2.33998
Very Fine	1.058591	1.1544	0.910179	2.34039
Extremely Fine	1.058507	1.15447	0.91043	2.34035

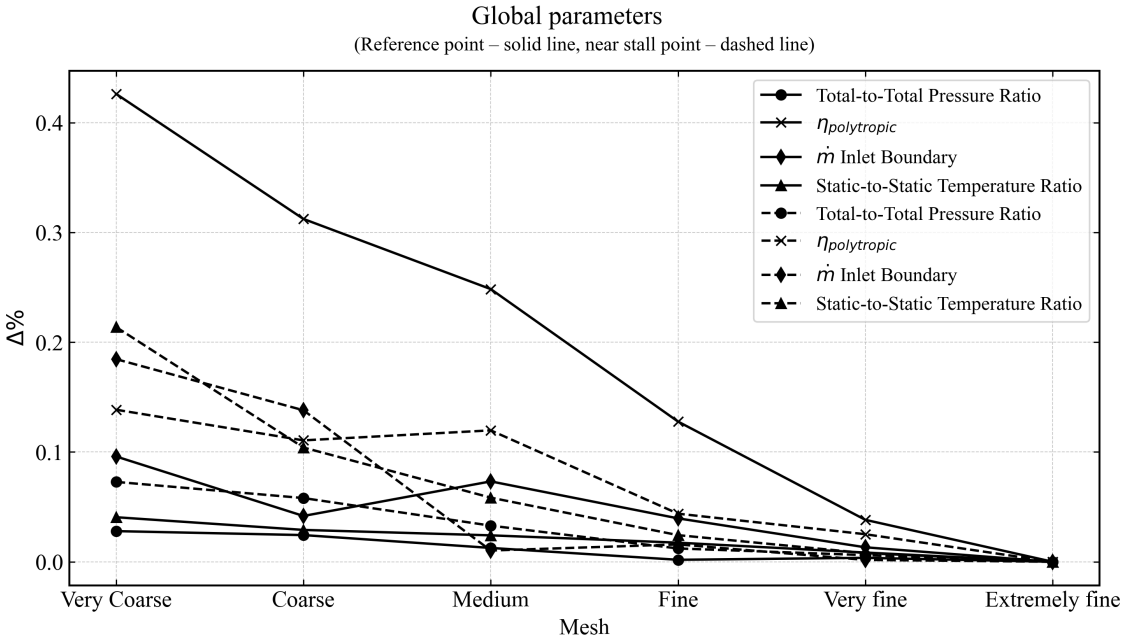

Figure 5.3: Convergence result of mesh study in subsonic flow.

With the sensors set up to mimic the Stuttgrad rig shown in Figure 4.2, the sensor closest to the leading-edge, SP7, was chosen as the target of this mesh study. The sensor location is shown in Figure 4.9, with a eroded geometry exhibiting a chord reduction of 1.5% from the test series shown in Figure 5.1. The static pressure, normalized with the results for the finest mesh, is shown in Figure 5.4.

It was decided that the fine mesh is sufficient for use in all subsequent investigations in this chapter, as it is considered to produce converged results for both global and local requirements.

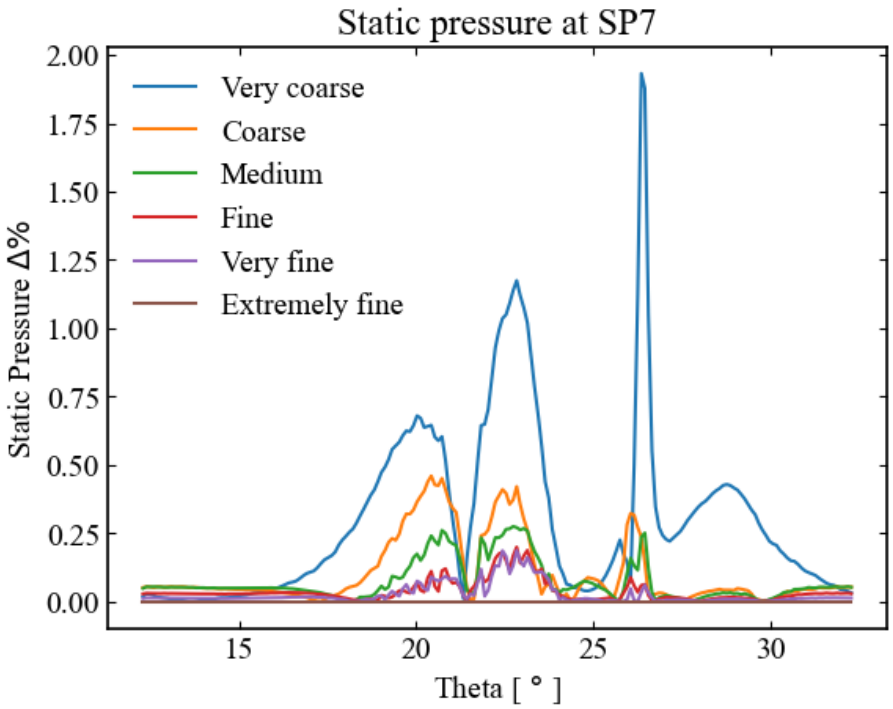

Figure 5.4: Static pressure Δ at SP7 for a worst-case erosion.

5.2 Result

This section presents the aerodynamic impact of a increasing erosion severity on the rotor blade under subsonic flow conditions. Key indicators such as polytropic efficiency, total pressure and total temperature ratio are analyzed to quantify the performance impact of erosion. The shift in operating points due to geometric degradation is examined, followed by a detailed investigation of loss mechanisms using spanwise entropy rise. Flow field characteristics are visualized through Mach number contours at 90% span, and pressure loading effects are assessed via spanwise pressure coefficient (C_p) distribution.

5.2.1 Aerodynamic Performance in Subsonic flow

Figure 5.5, Figure 5.6, and Figure 5.7 summarizes the aerodynamic effects of progressive leading-edge erosion on compressor rotor performance at subsonic operating conditions. Displayed are trends in polytropic efficiency (η_p), total pressure rise, and total temperature rise for both the reference point (REFP) and near-stall point (NSP), these values are shown relative to the nominal case. Observations reveal a reduction in efficiency with increasing erosion severity, highlighting how additional shaft work is predominantly converted into losses rather than useful pressure rise. Erosion leads to a decrease in polytropic efficiency at both operating points, with a total reduction of 1.06 percentage points at REFP and 2.16 percentage points at NSP in the most severe case (1.5% chord reduction at the rotor tip). This drop is primarily attributed to changes in the total pressure and temperature ratios: for the reference

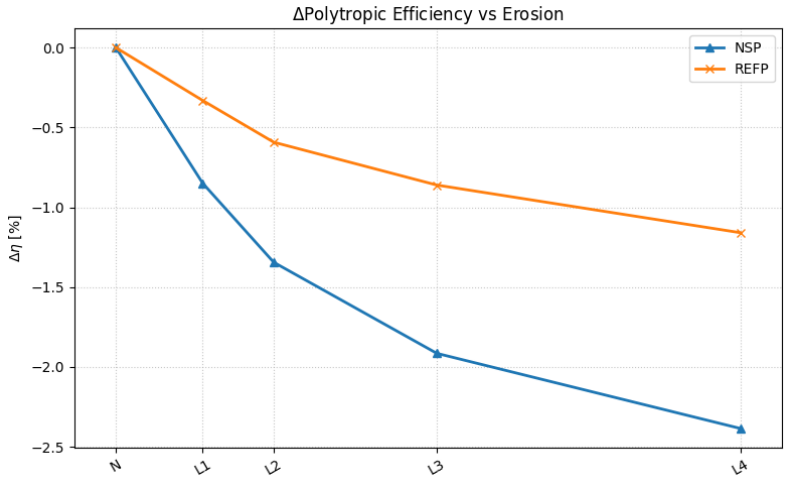

Figure 5.5: Relative change (%) in polytropic efficiency for REFP and NSP.

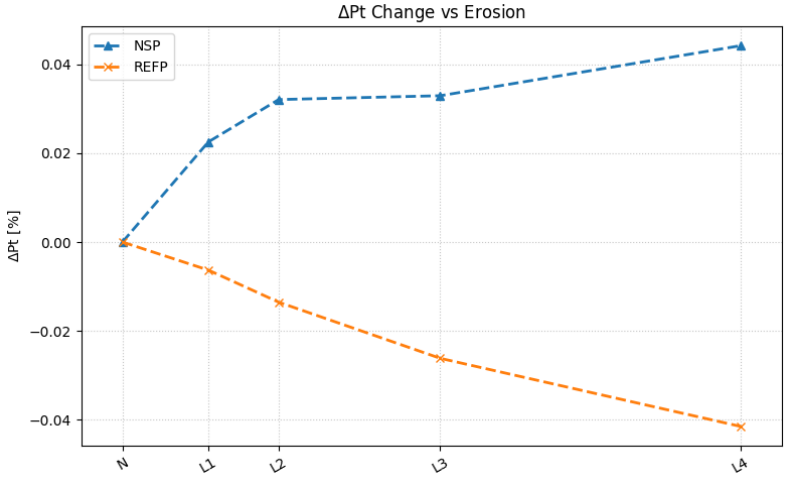

Figure 5.6: Relative change (%) in total pressure ratio for REFP and NSP.

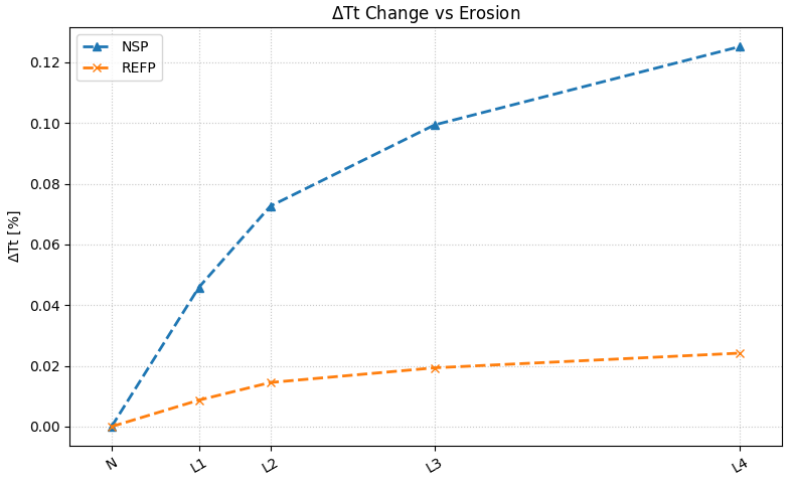

Figure 5.7: Relative change (%) in total temperature ratio for REFP and NSP.

point (REFP), the total pressure ratio decreases while the total temperature ratio increases. For NSP, the total pressure ratio increases, but not to the same extent as the temperature ratio. Both operating points indicate that additional work is being done to the flow, but not effectively converted into total pressure rise. Instead, the extra work manifests as increased irreversible losses, likely associated with enhanced dissipation mechanisms such as boundary layer separation and secondary flows. A summary of the polytropic efficiency degradation is presented in Table 5.5.

Table 5.5: Polytropic efficiency decrease for REFP and NSP at different levels of erosion.

Erosion level	**REFP (%)**	**NSP (%)**
1	-0.30	-0.77
2	-0.54	-1.22
3	-0.79	-1.74
4	-1.06	-2.16

5.2.2 Operating Point Shift

At constant rotational speed and average back pressure, the compressor rotor's operating point shifts leftward from its nominal position when leading-edge erosion is introduced.

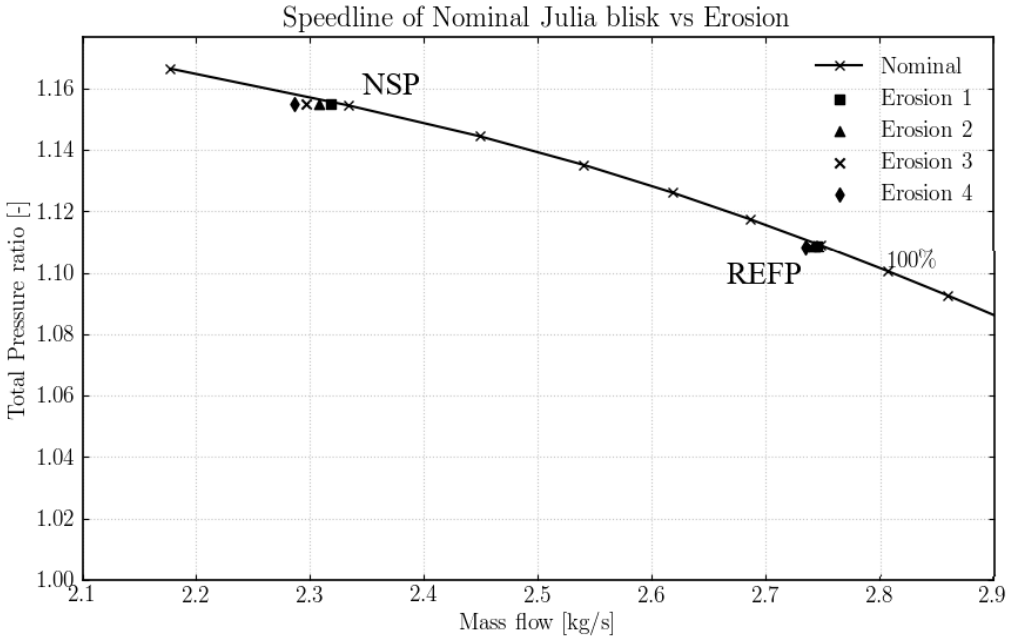

Figure 5.8: Operating points of eroded cases compared to the nominal speedline.

A reduction in mass flow can be observed in the figure above, with changes in total pressure present in the same figure and more visible in Figure 5.6. In Figure 5.6, the

pressure ratio decreases for REFP, while it increases for NSP relative to the nominal blade. These trends, i.e., changes in mass flow and total pressure rise, indicate that erosion not only affects local aerodynamic performance but also alters the global operating characteristics of the compressor.

5.2.3 Spanwise Entropy Rise as an Indicator of Loss Distribution

To illustrate the spatial distribution of aerodynamic losses, the spanwise variation of entropy rise across the rotor blade at the reference point (REFP) and near-stall point (NSP) is shown in Figures 5.9 and 5.10, respectively.

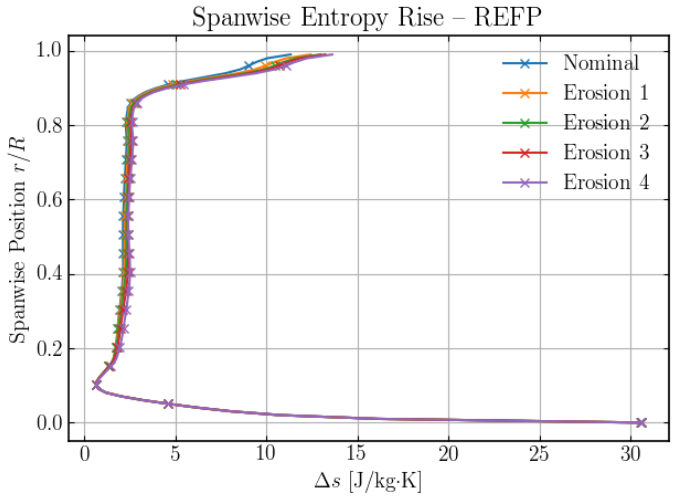

Figure 5.9: Spanwise entropy rise over the rotor blisk at REFP.

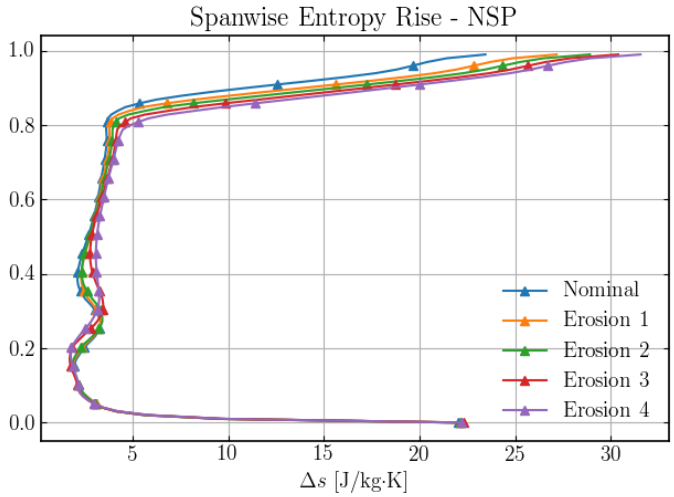

Figure 5.10: Spanwise entropy rise over the rotor blisk at NSP.

To localize the regions where losses occur, spanwise profiles of entropy rise are examined. For the reference point (REFP), entropy differences between the nominal

blade and the eroded ones remain relatively constant up to approximately 90% span, beyond which deviations begin to appear as erosion severity increases. At the near stall point (NSP), significant differences in entropy rise are observed between 20% and 50% span for erosion levels 3 and 4, along with consistent deviations above 80% span across all erosion cases. The entropy rise is particularly pronounced in the near-tip region for both operating points, indicating that tip-region phenomena dominate the loss mechanisms. These findings prompted a more detailed investigation of the flow field in the upper span region of the rotor blade.

5.2.4 Mach Number Contours at 90% Span

In Figures 5.13 and 5.16, Mach number and axial velocity contours at 90% span are presented for both the nominal blade geometry and the most severely eroded case at the reference point (REFP).

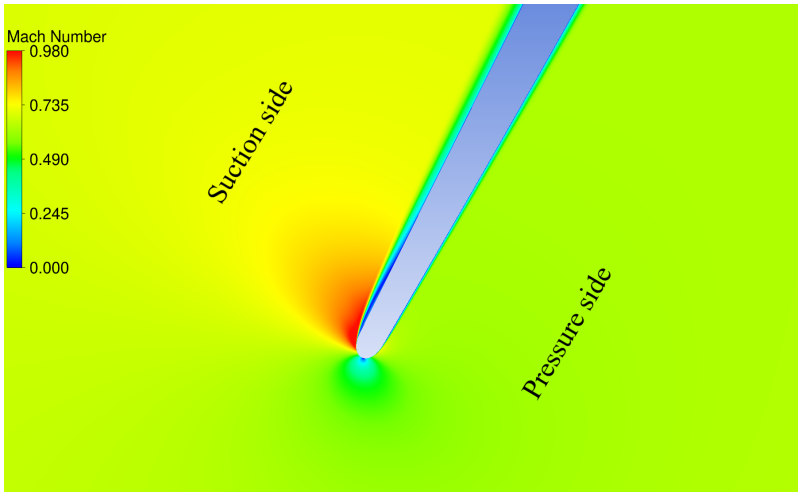

Figure 5.11: Nominal blade.

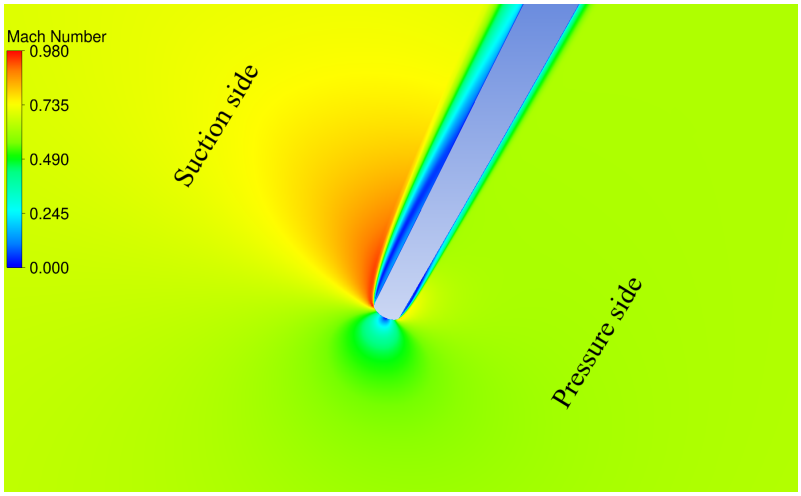

Figure 5.12: Level 4 eroded blade.

Figure 5.13: Comparison of Mach number flow fields at 90% span at REFP between the nominal and eroded blade geometries.

In Figure 5.14, a small separation bubble is visible just downstream of the leading edge on the suction side of the nominal blade. As erosion increases, the leading edge becomes more blunt, causing the flow to accelerate locally over the suction surface to adapt to the altered geometry. This intensifies the adverse pressure gradient near the leading edge, resulting in a larger separation bubble in the eroded case. Additionally, early signs of separation begin to appear on the pressure side, where a much smaller separation bubble—compared to the suction side—develops in the eroded blade. This is due to local flow acceleration over the pressure surface as well, as seen in the figure.

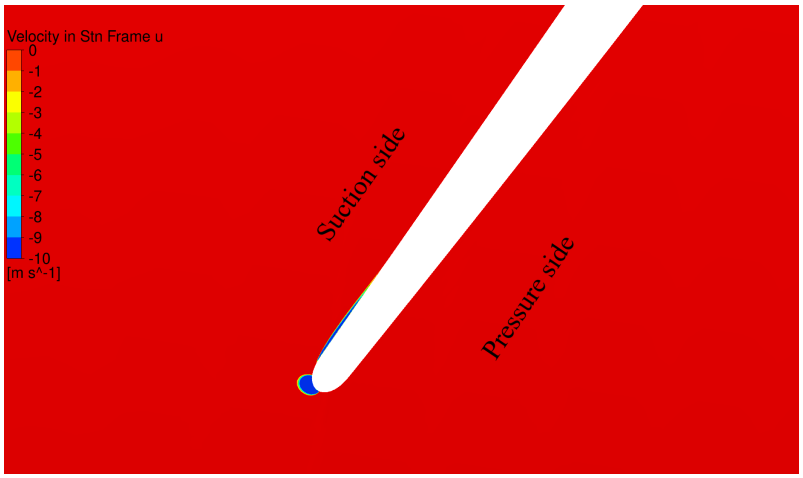

Figure 5.14: Nominal blade.

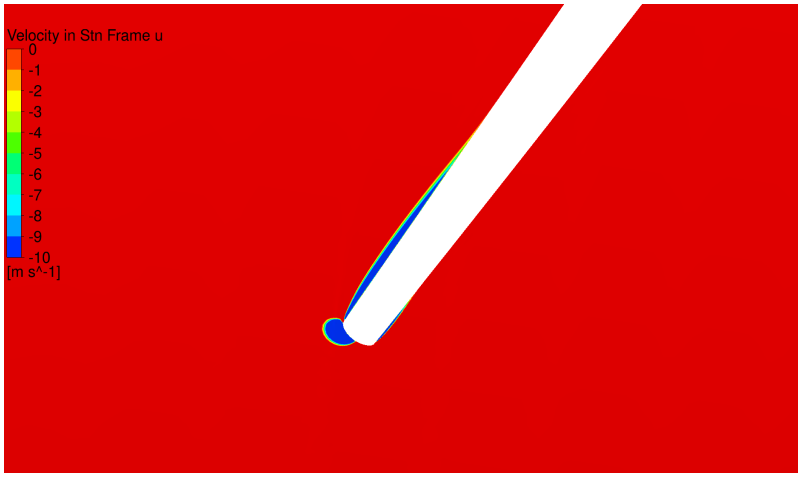

Figure 5.15: Level 4 eroded blade.

Figure 5.16: Axial velocity contours at 90% span at REFP for the nominal and eroded blade geometries.

As a consequence of the larger separation bubble in the eroded case, the reattachment point shifts further downstream, and the boundary layer becomes thicker after reattachment, as observed in Figure 5.13.

Furthermore, the stagnation region at the leading edge expands slightly in the eroded

case. These changes illustrate how leading-edge erosion alters the local flow behavior, ultimately contributing to the degradation of aerodynamic performance.

In Figures 5.19 and 5.22, Mach number and axial velocity contours at 90% span are presented for both the nominal blade geometry and the most severely eroded case at the near-stall point (NSP).

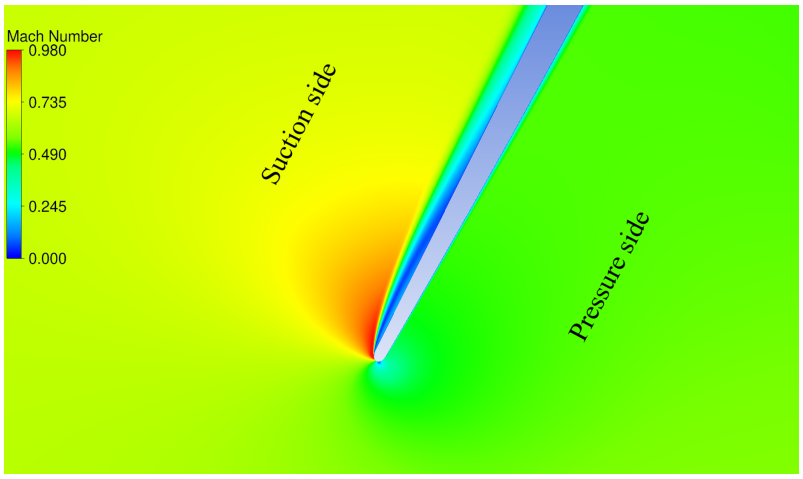

Figure 5.17: Nominal blade.

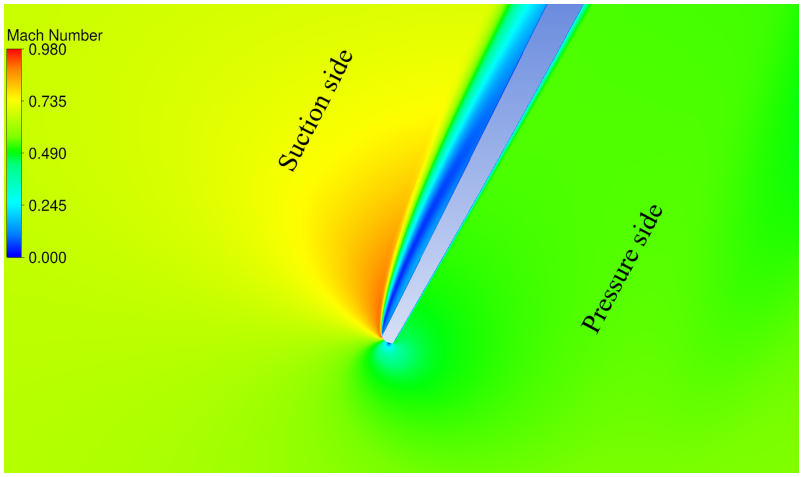

Figure 5.18: Level 4 eroded blade.

Figure 5.19: Comparison of Mach number flow fields at 90% span at NSP between the nominal and eroded blade geometries.

At the near-stall point (NSP), the rotor operates under higher incidence angles, which promote a larger separation region on the suction side compared to the reference point (REFP). Combined with the increased leading-edge bluntness due to erosion, this significantly amplifies the separation bubbles already observed at REFP. In the eroded case, the separation bubble on the suction surface is notably larger, and the boundary layer after reattachment appears thicker as well.

However, no signs of separation are observed on the pressure side at NSP, in con-

trast to REFP. This suggests that under near-stall conditions, at higher incidence angle, the flow behavior due to erosion becomes increasingly dominated by suction-side phenomena, with loss-driving mechanisms shifting further toward the suction surface of the blade.

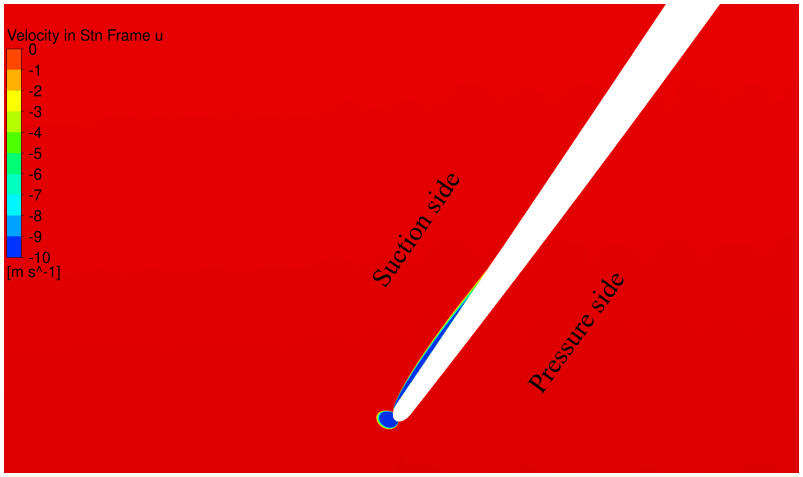

Figure 5.20: Nominal blade.

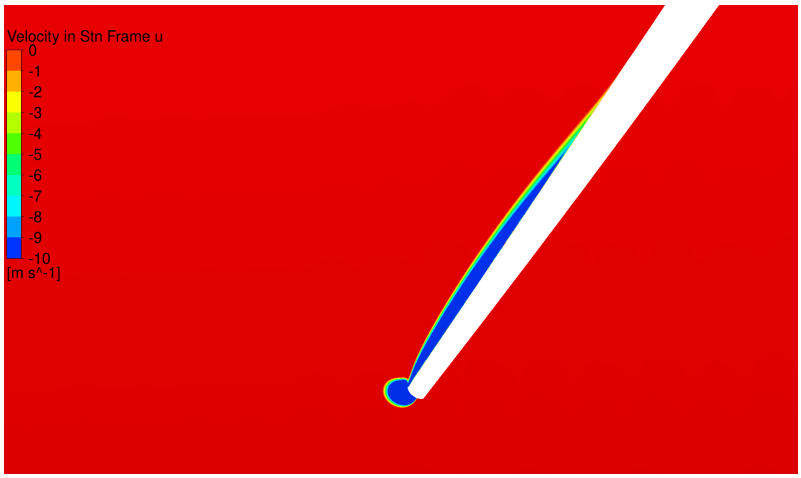

Figure 5.21: Level 4 eroded blade.

Figure 5.22: Axial velocity contours at 90% span at NSP for the nominal and eroded blade geometries.

5.2.5 Spanwise Pressure Coefficient (C_p) Distribution

Figures 5.23 illustrate the static pressure coefficent distribution at the 90% span location for both the reference point (REFP) and near-stall point (NSP). The left column focuses on the leading edge region (0–25% normalized chord), while the right column shows the distribution over the entire suction and pressure sides.

At higher spans, i.e at 90% span—the suction side is affected at both operating points. Increasing erosion severity leads to a reduced ability of the flow to recover

after the suction peak just downstream of the leading-edge. This behavior is attributed to the growth of the separation bubble seen in the Figures 5.16 and 5.22, which becomes more pronounced with increasing leading-edge erosion.

At the reference point (REFP), a similar behavior can be observed on the pressure side, as shown in Figure 5.23. The differences seen just downstream of the leading edge between the cases are attributed to a growing separation bubble, as illustrated in Figure 5.16.

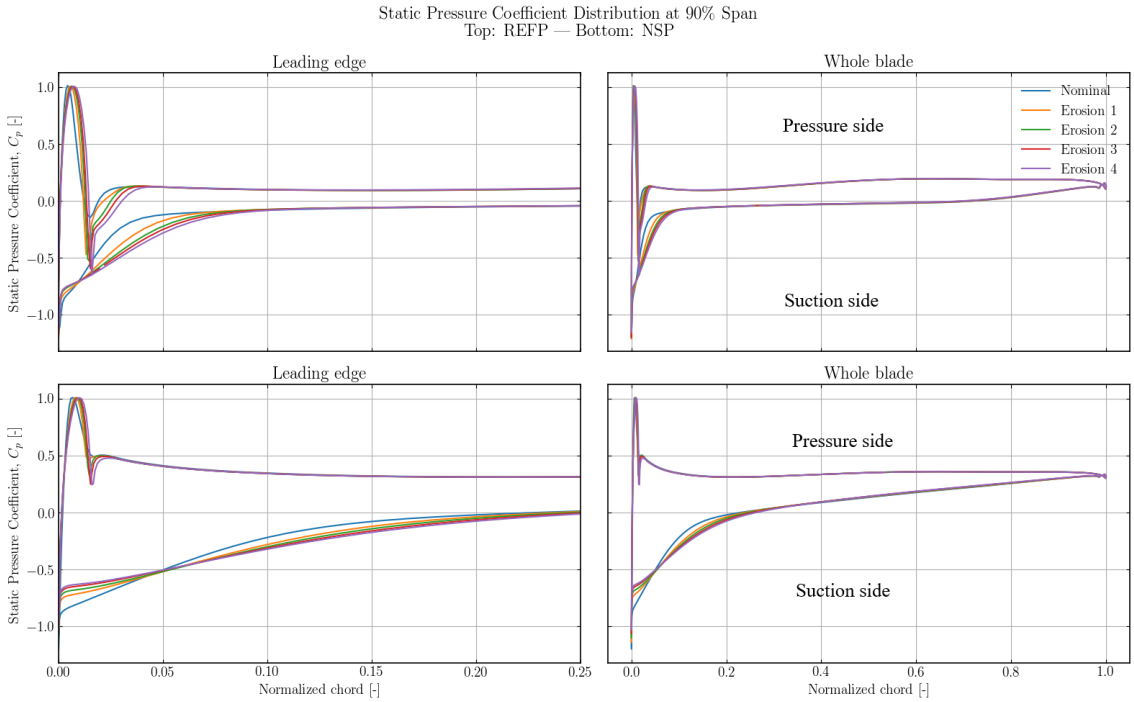

Figure 5.23: Static pressure coefficient distribution at 90% span for nominal and eroded blades at REFP and NSP.

6

Transonic Flow (R134a)

Building on the subsonic erosion flow phenomena identified in Chapter 5, this chapter investigates the effects of leading-edge erosion under transonic flow conditions. The transonic operating regime introduces distinct flow characteristics compared to subsonic conditions. As flow velocities approach Mach 1, supersonic regions begin to form, terminating in shock waves. These shocks introduce additional loss mechanisms that intensify as the severity of leading-edge erosion increases.

6.1 Method

This section outlines the methodology used to investigate rotor performance under transonic flow conditions using R134a as the working fluid. The transition from standard atmospheric air to R134a is representative for the experimental setup planned for future test campaigns at the University of Stuttgart rig, and enables the rotor to operate closer to its intended design conditions. The approach includes inlet boundary profiles derived from full-domain CFD studies, the selection of operating points based on speedline analysis, and a detailed mesh sensitivity study to ensure numerical accuracy. Additionally, the range of erosion severity is extended beyond that considered in the subsonic cases.

6.1.1 R134a (Heavy gas)

In this chapter, idealized R134a (1,1,1,2-Tetrafluoroethane) was used as the working fluid for all calculations. This marks a shift from Chapter 4, where standard atmospheric air based on ISA sea-level conditions was used. The transition to R134a enables a more representative analysis of the intended application environment. Notably, the Julia Blisk [4.1] is designed for transonic flow conditions, and the use of R134a supports achieving the design tip Mach number at a lower tip velocity compared to air.

This, in turn, allows for lower rotational speeds, which reduces mechanical stresses on components in a real test rig. Consequently, R134a was selected to better match the operating conditions of the forthcoming rig test campaign at the University of Stuttgart. A comparison of key fluid properties is presented in Table 6.1.

Table 6.1: Comparison of thermophysical properties between R134a and ISA air at 300 K.

Property	R134a @ 300 K, 50 kPa	ISA Air @ Sea Level	Units
C_p	0.860	1.005	kJ/kg·K
γ	1.112	1.40	–
Density (ρ)	1.93	1.225	kg/m^3
Speed of Sound (a)	163	340	m/s
Gas Constant (R)	81.5	287.1	J/kg·K

6.1.2 Inlet Conditions

The inlet boundary conditions were modified to match the actual full setup in the compressor rig at the University of Stuttgart. Without adding upstream inlet guide vanes into the domain, which would affect the incoming flow field to the rotor blade, inlet profiles of total pressure in the stationary frame and velocity components (Axial, Radial, and Tangential) were given from previous conducted CFD studies with the full geometry of the test domain. Since the endwalls are horizontal at the inlet, the radial component was set to zero. The values of the velocity components (Axial and Tangential) have been normalized with the absolute velocity, and all the inlet profiles used are presented in Figure 6.1. The inlet total temperature was adjusted to a constant total temperature of 300 k and the rotational speed to 17, 105 RPM to match the intended conditions at the rig.

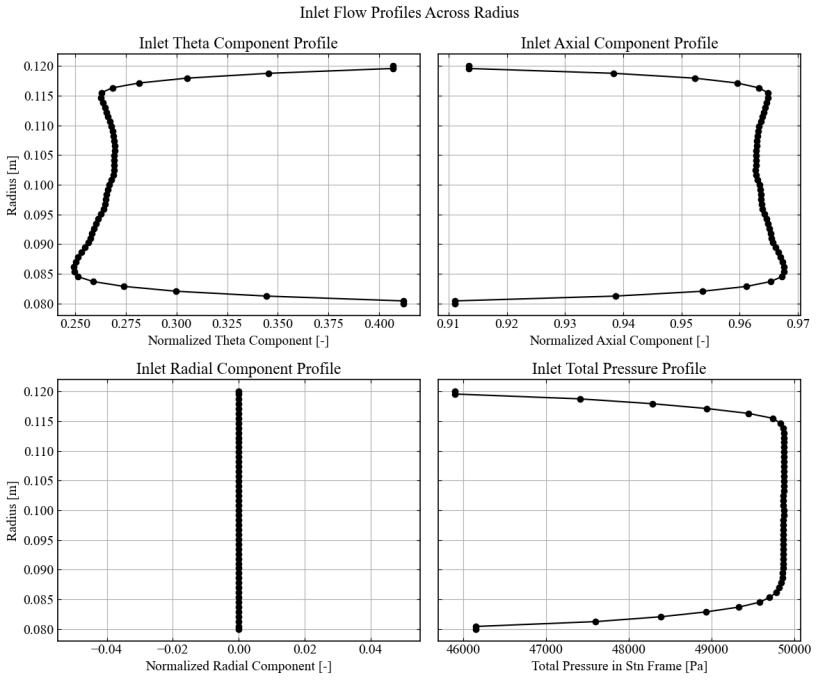

Figure 6.1: Inlet flow profiles across the radius.

6.1.3 Operational Points

Figure 6.2 shows a speedline using R134a as the working fluid. Compared to the subsonic speedline presented in Figure 5.2, both the total pressure rise and the mass flow rate at a constant speed of 17,105 RPM have increased, as an effect of changing the working fluid properties.

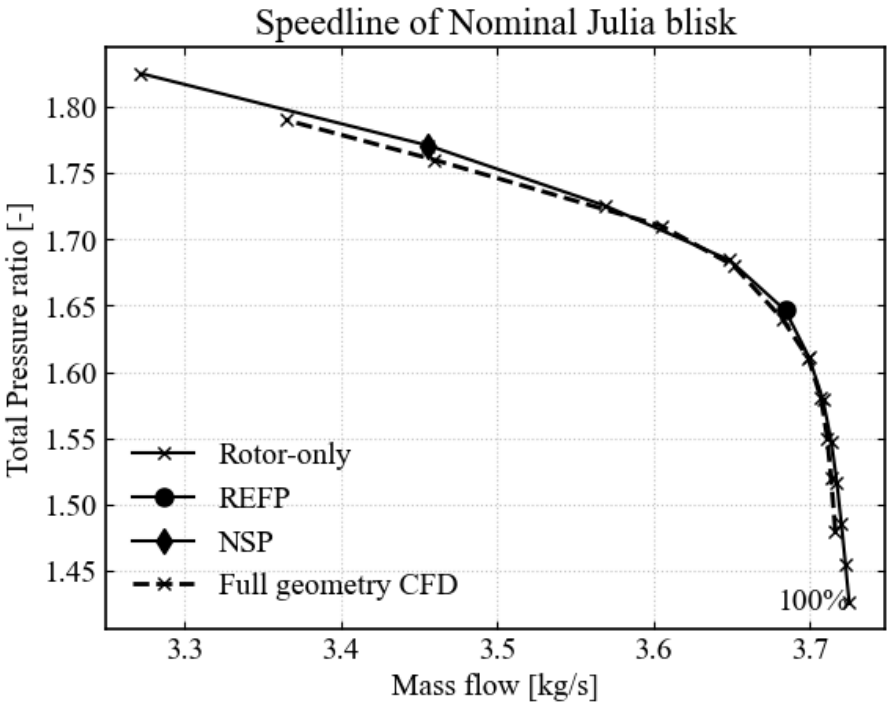

Figure 6.2: Speedline using R134a at 17,105 RPM.

The total-to-total pressure speedline from the rotor-only domain used in this study is compared to the speedline obtained from a previous investigation of the full CFD setup with R143a in the CoFAS project. The agreement between the two confirms that the inlet profiles are working as intended, as the rotor-only speedline lies close to the full geometry speedline. The two operational points of interest, reference point (REFP) and near-stall point (NSP), are marked in the figure. The corresponding values of mass flow and static outlet pressure for these points are listed in Table 6.2.

Table 6.2: Mass flow and static outlet pressure at operational points

Operational Point	Mass Flow (kg/s)	Static Outlet Pressure (kPa)
Reference point (REFP)	3.68	57
Near-stall point (NSP)	3.46	60

6.1.4 Mesh study

In this mesh study, the very coarse mesh was excluded due to its faliure to converge under transonic flow conditions. The global performance paramters for the reference point (REFP) and near stall point (NSP) are presented in Table 6.3 and Table 6.4, respectively. Figure 6.3 illustrates the convergence of these parameters, nomalized with respect to the results obtained using the finest mesh.

Table 6.3: Mesh Study Results REFP

Mesh Size	**P_0 Ratio**	**T_0 Ratio**	η_{poly}	$\dot{m}$
Coarse	1.64353	1.05381	0.954703	3.67622
Medium	1.64478	1.05387	0.955283	3.68022
Fine	1.64568	1.0539	0.955704	3.68208
Very Fine	1.64607	1.05392	0.955894	3.68295
Extremely Fine	1.64627	1.05392	0.956067	3.68306

Table 6.4: Mesh Study Results NSP

Mesh Size	**P_0 Ratio**	**T_0 Ratio**	η_{poly}	$\dot{m}$
Coarse	1.76952	1.06294	0.941691	3.40975
Medium	1.76937	1.06265	0.945759	3.445
Fine	1.76964	1.06251	0.948089	3.45982
Very Fine	1.77005	1.06245	0.949323	3.46648
Extremely Fine	1.77043	1.06245	0.949757	3.4685

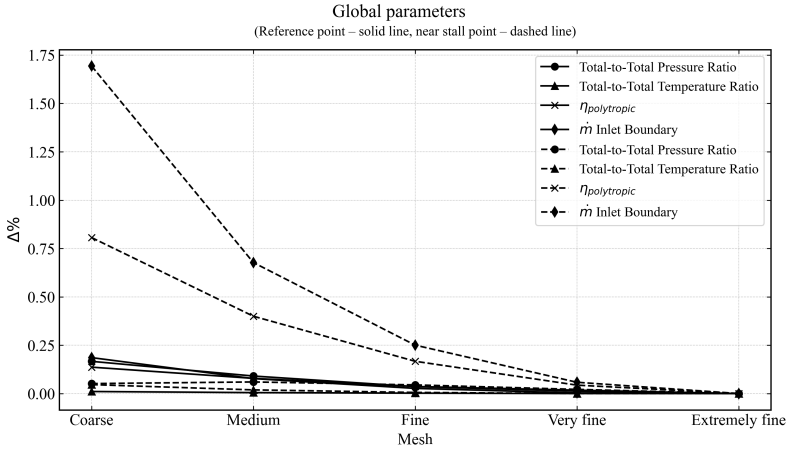

Figure 6.3: Convergence of global parameters in the mesh study under transonic flow conditions.

A mesh study was also conducted for an eroded geometry, using erosion level 6, which corresponds to a chord reduction of 6.4% at the blade tip, as shown in Figure 6.5. The static pressure at the shroud casing over the rotor is shown at sensor location SP7 (see Figure 4.2), normalized with respect to the finest mesh, is presented in Figure 6.4.

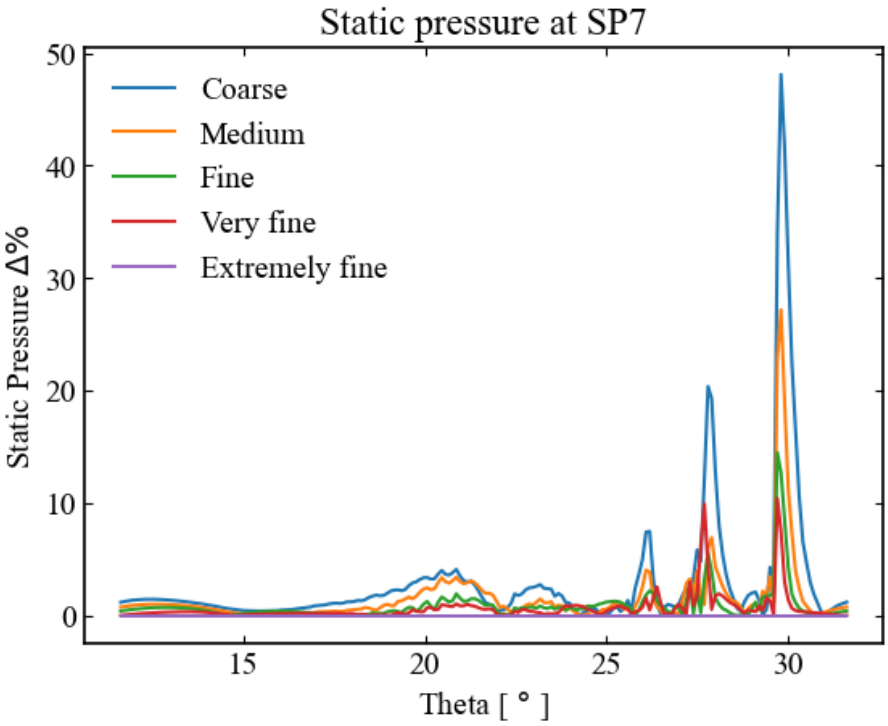

Figure 6.4: Static pressure difference at SP7 for the worst-case erosion scenario

Based on the results, the fine mesh was deemed sufficient for all subsequent investigations in this chapter, as it provides converged results for both global and local flow characteristics.

6.1.5 Erosion

The erosion levels that is being investigated have in this chapter been extended with two new cases, doubling the erosion severity two times more. The maximum chord reduction at the blade tip are now 6.4%, compared to 1.5% from the subsonic test cases. The overall geometrical deviations for each test case at 10%, 30%, 50% and 90% spans are shown in Figure 6.5.

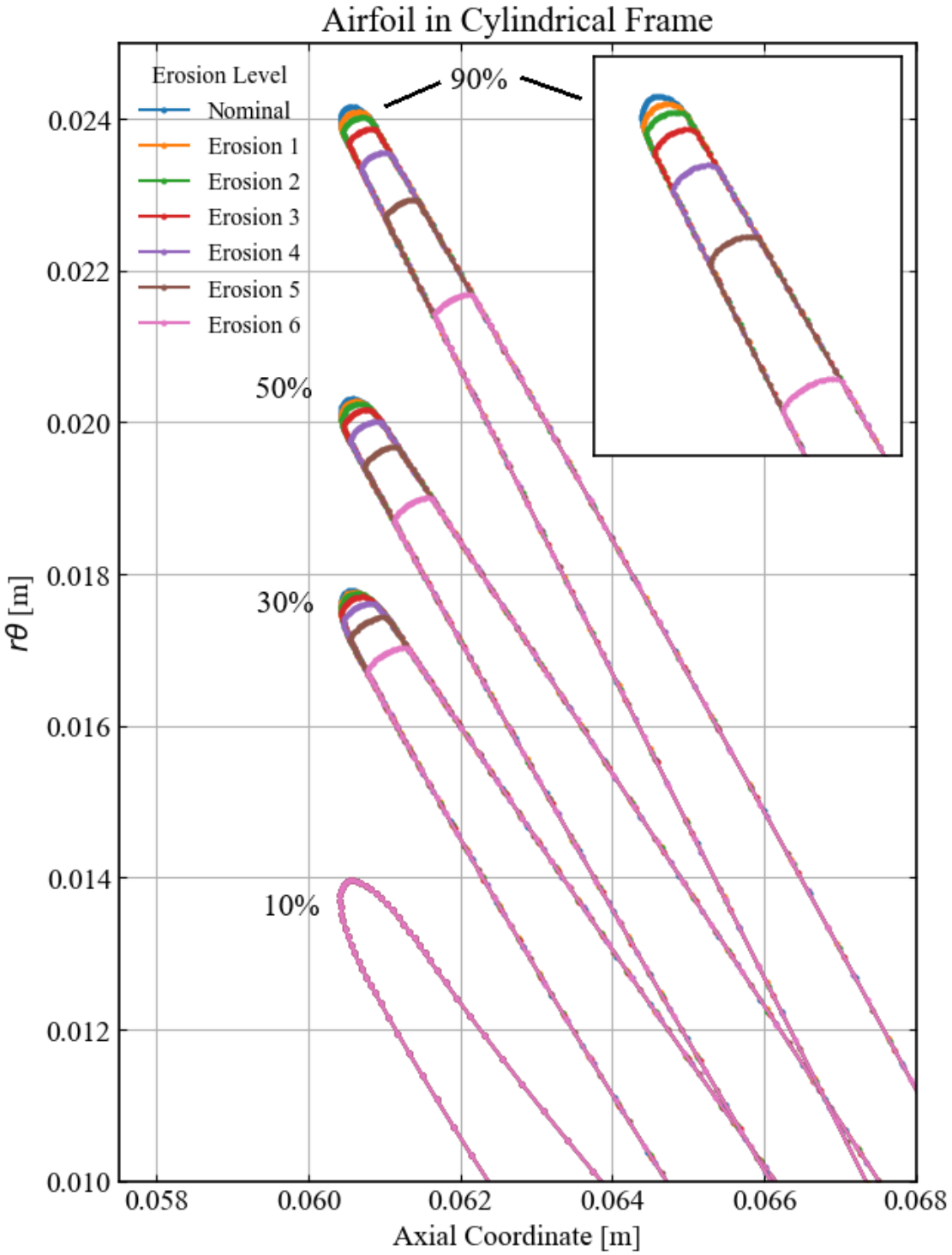

Figure 6.5: Increasing erosion severity on the leading-edge for the rotor blade.

6.2 Results

The transonic analysis is conducted in a similar manner to the subsonic investigation, enabling a direct comparison between the nominal and eroded cases. In

this chapter, the presence of shock waves introduces additional complexity, which is examined through Mach number contour plots and spanwise distributions of the static pressure coefficient (C_p). Furthermore, the entropy-based loss analysis is extended by including the entropy difference between eroded and nominal blades at a spanwise location downstream of the rotor leading-edge. This addition enhances the understanding of localized loss generation and its correlation with erosion severity.

6.2.1 Aerodynamic Performance in Transonic flow

Figure 6.6, Figure 6.7, and Figure 6.8 present changes in polytropic efficiency, total pressure ratio, and total temperature ratio, respectively, for the reference point (REFP) and near-stall point (NSP). These values are shown relative to the nominal case across increasing erosion severity levels.

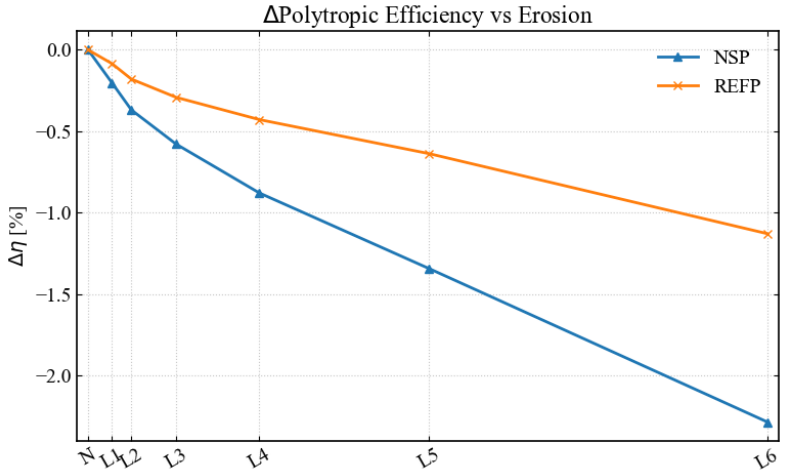

Figure 6.6: Relative change (%) in polytropic efficiency for REFP and NSP.

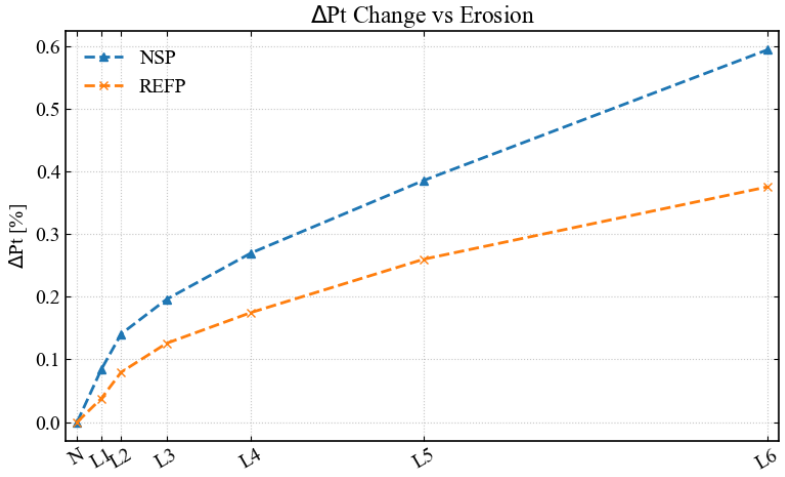

Figure 6.7: Relative change (%) in total pressure ratio for REFP and NSP.

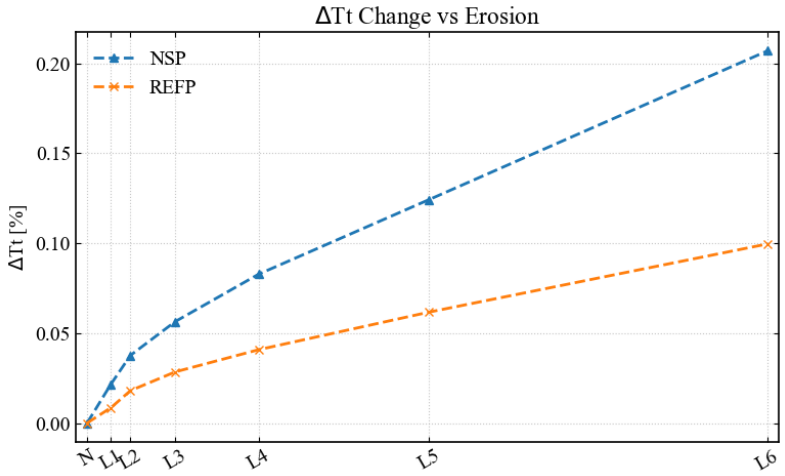

Figure 6.8: Relative change (%) in total temperature ratio for REFP and NSP.

For both the reference point (REFP) and near-stall point (NSP), the degradation in polytropic efficiency exhibits an approximately linear trend with erosion severity ranging from level 3 to level 6. The maximum reductions were observed as a decrease of 1.08% percentage points for REFP and 2.17% for NSP. Similarly, the total pressure and total temperature ratios increase approximately linearly from erosion level 3 to 6, following a comparable trend. These changes reflect the growing aerodynamic loading and flow distortion associated with leading-edge erosion. A detailed summary of the efficiency degradation trends is provided in Table 6.5

Table 6.5: Polytropic efficiency decrease for REFP and NSP at different levels of erosion.

Erosion level	**REFP** (%)	**NSP** (%)
1	-0.08	-0.19
2	-0.17	-0.35
3	-0.28	-0.55
4	-0.41	-0.83
5	-0.61	-1.27
6	-1.08	-2.17

Going futher in the investigation, erosion levels 4–6 were selected for detailed analysis, as they exhibit the most significant impact on aerodynamic performance, as shown in Table 6.5.

6.2.2 Operation Point Shift

Figure 6.9 presents the nominal speedline at the design speed of $17,105,\text{rpm}$ and illustrates how blade erosion shifts the operating points—REFP and NSP—relative to the nominal blade.

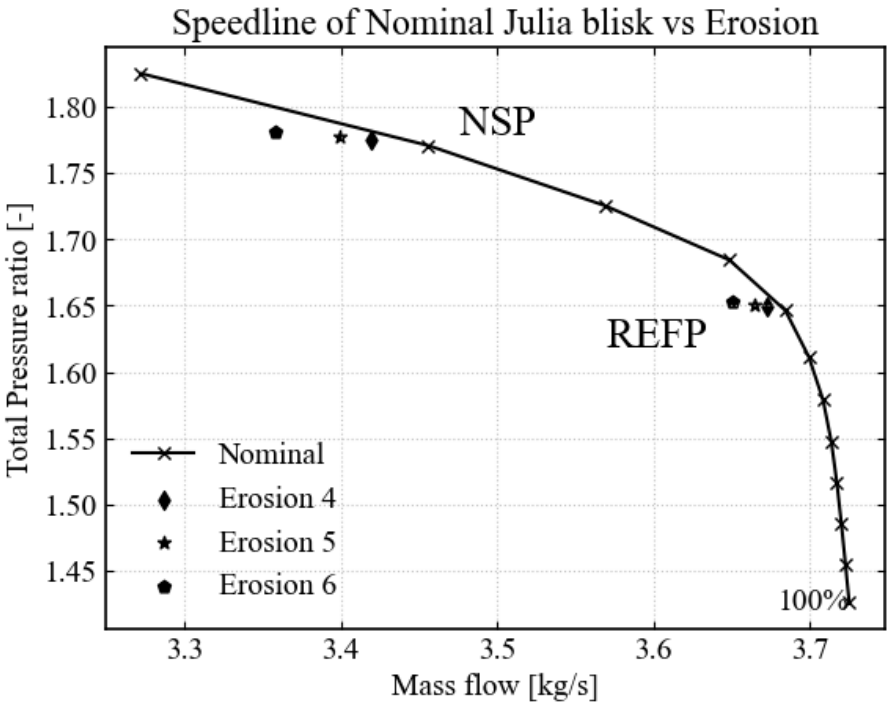

Figure 6.9: Operational point shift at design speed for REFP and NSP.

Keeping back-pressure fixed at REFP and NSP and maintaining the same shaft speed, increasing erosion severity drives the operating points leftward (lower mass-flow rate) and slightly upward (higher total-pressure rise) relative to the nominal operating point. This shift moves the compressor closer to stall and consequently reduces the available surge margin.

6.2.3 Mach Number Contours at 90% Span — Shock Structure

To investigate the effect of leading-edge erosion on shock structures and associated loss mechanisms, Figure 6.10 and 6.11 presents a comparison of Mach number contours at 90% span for the nominal and eroded blade geometries at the reference point (REFP) and near-stall point (NSP).

Mach-number contours show that, in the eroded case for both REFP and NSP, the bow shock (Point A) becomes more normal relative to the incoming flow, creating a larger subsonic region ahead of the leading-edge. At Point B for both REFP and NSP—where the bow shock meets the suction-side shock to form a lambda-shock structure—the shock curvature straightens slightly, aligning a greater portion of the incoming flow perpendicular to the shock. As a result, the normal velocity component, and thus the influence of the shocks increases, indicating that the overall shock system has both intensified and migrated slightly upstream.

At point C, for REFP, a shock is observed downstream of the leading-edge on the pressure side of the blade, as local velocities increases when the flow curve around

the more blunt profile for the eroded case, the shock occur close to the leading-edge, and subsequently the extend of the local high velocity region decrease on the pressure side.

Flow separation occurs downstream of the lambda foot at the reference point (REFP), at point B. At this location, the separation point shifts upstream, and the overall separated region is slightly reduced for the eroded blade. The subsequent boundary layer after the separation on the suction side does not thicken for the eroded case; instead, it slightly decreases, as can be observed in figure 6.12

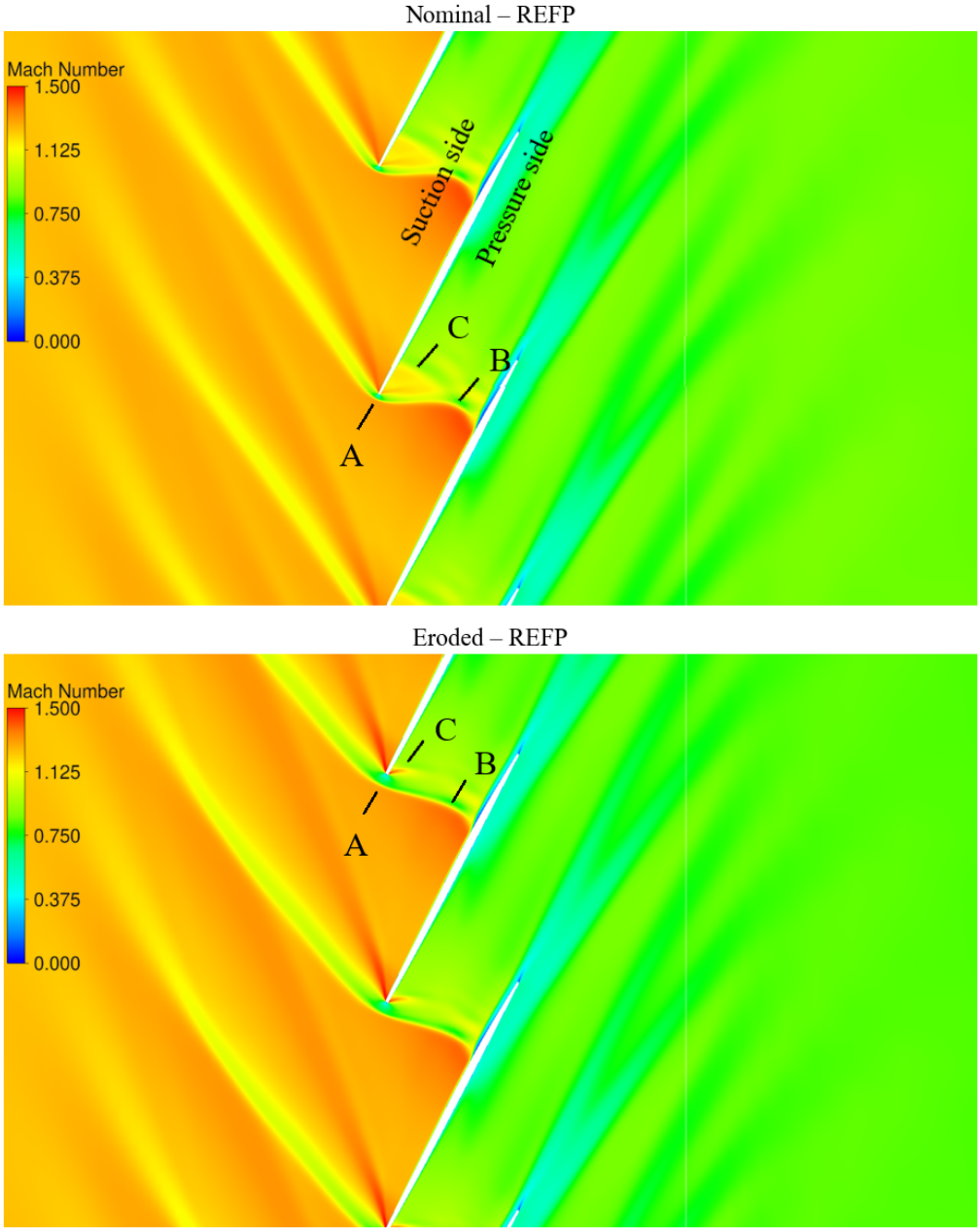

Figure 6.10: Comparison of Mach number flow fields at 90% span for the nominal and eroded blades at reference point (REFP) and near-stall point (NSP).

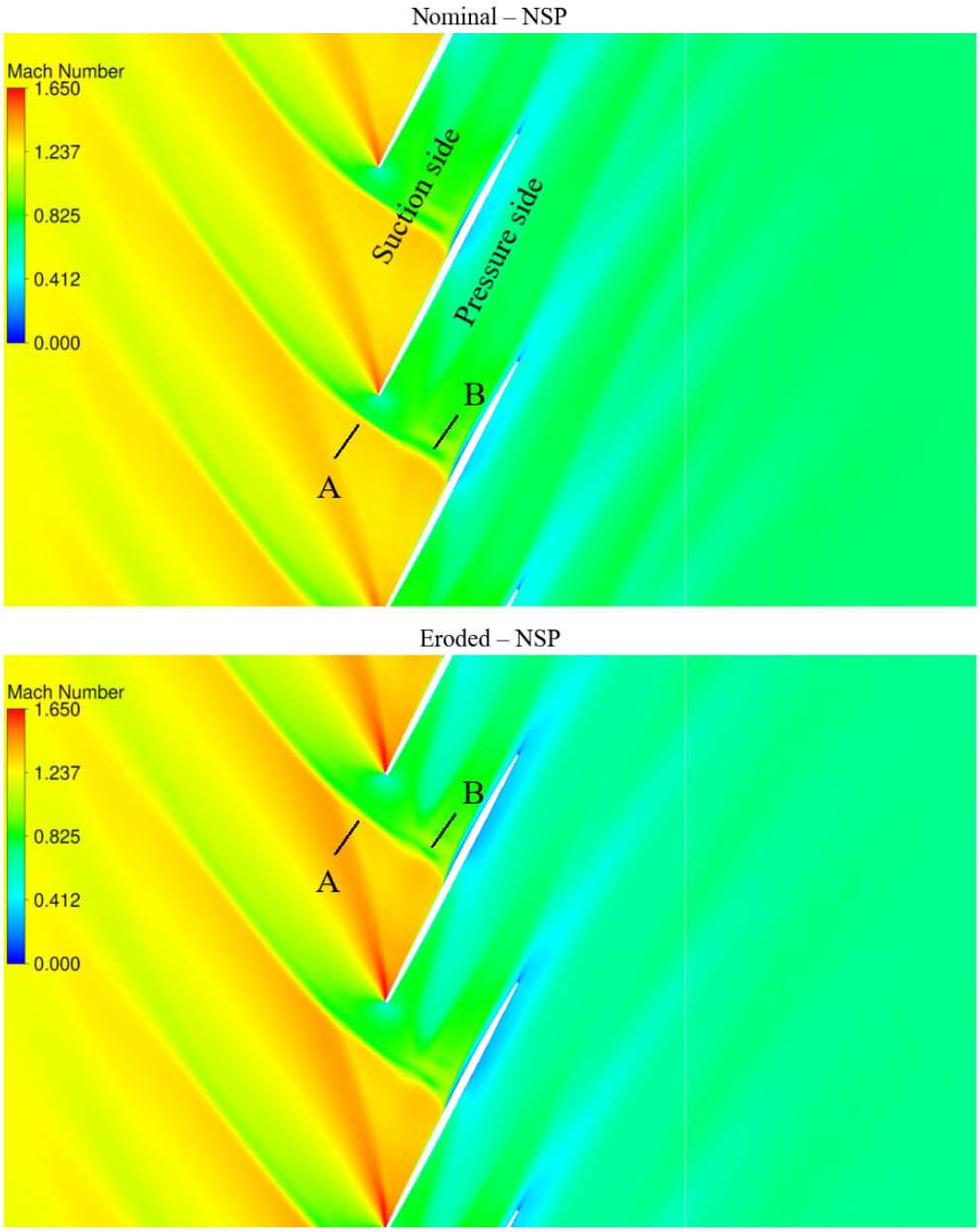

Figure 6.11: Comparison of Mach number flow fields at 90% span for the nominal and eroded blades at REFP and NSP.

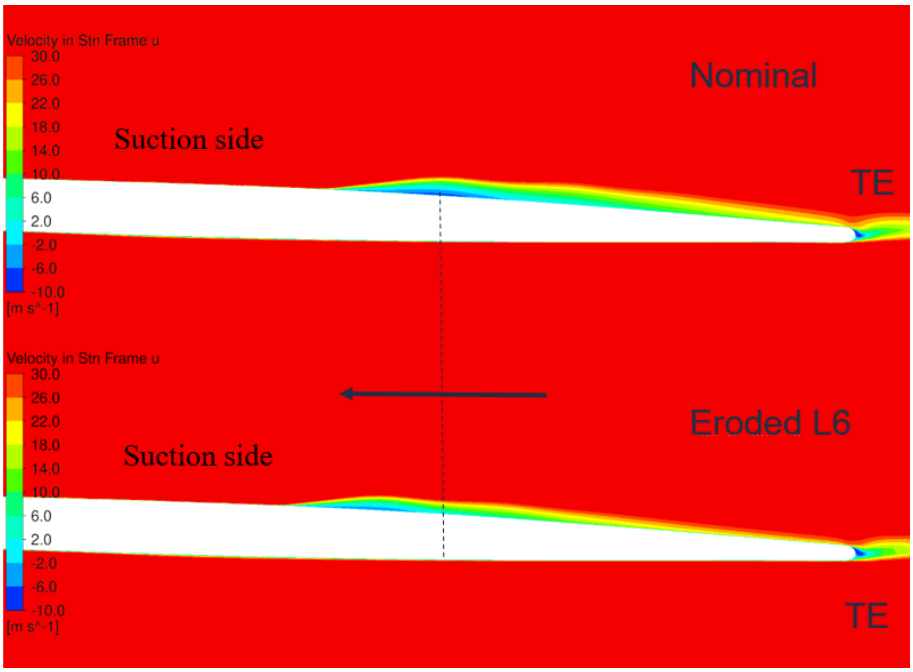

Figure 6.12: Comparison of axial velocity field at 90% span for the nominal and eroded blades at REFP.

6.2.4 Spanwise Pressure Coefficient (C_p) Distribution

To assess the impact of leading-edge erosion on the pressure loading over the blade surface, Figure 6.13 and 6.14 presents the static pressure coefficient distribution at 90% span for both the reference point (REFP) and near-stall point (NSP). The left column focuses on the leading-edge region (0–25% normalized chord), while the right column shows the distribution over the entire suction and pressure side.

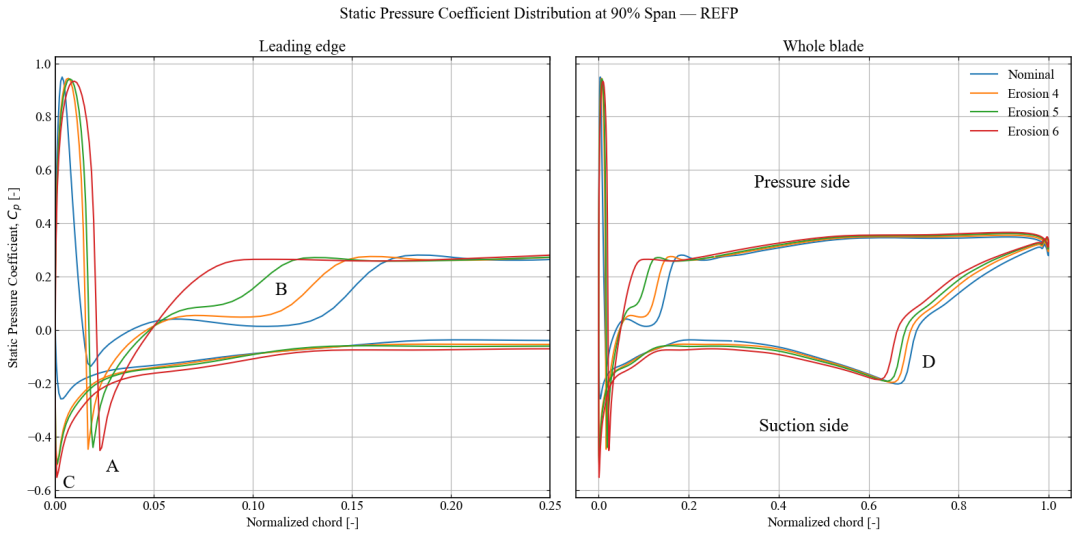

Figure 6.13: Static pressure coefficient distribution at 90% span for nominal and eroded blades at REFP and NSP.

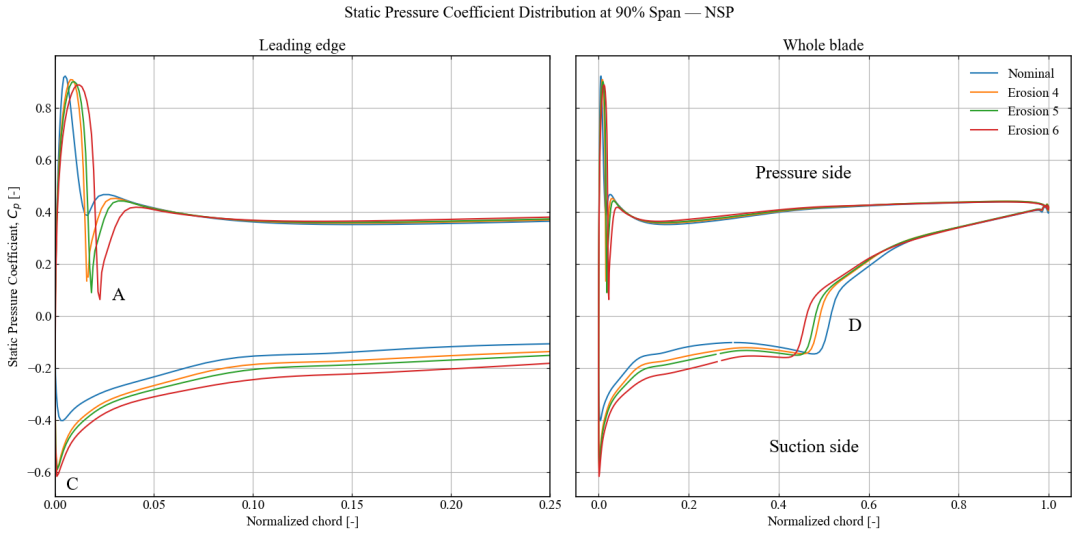

Figure 6.14: Static pressure coefficient distribution at 90% span for nominal and eroded blades at REFP and NSP.

From the figures, at point A, it can be observed that as the flow turns toward the pressure side, the increased velocity over the leading-edge—due to its curvature—creates a negative pressure dip that becomes more pronounced with erosion. At the reference point (REFP), at point B, this local increase in velocity subsequently forms a shock, which shifts upstream on the pressure side for the eroded cases.

On the suction side, erosion leads to an increase in the suction peak at point C, and the resulting adverse pressure gradient becomes steeper. Also a slightly lower static pressure can be observed along the suction surface downstream of the peak in the eroded cases. Around 65% and 50% chord for REFP and NSP respectively, at point D, the suction-side shock is observed. With increasing erosion, the shock location shifts upstream along the blade surface, as indicated by the leftward movement of the sharp rise in static pressure along the suction side.

These trends highlight the sensitivity of the local pressure distribution to leading-edge erosion, especially at flow features such as the suction peaks and shock system.

6.2.5 Spanwise Entropy Rise as an Indicator of Loss Distribution

To illustrate the radial distribution of aerodynamic losses, the spanwise variation of entropy rise across the rotor blade is presented in Figures 6.15 and 6.16. As observed in the figures, the tip region remains the dominant contributor to entropy generation for both REFP and NSP, consistent with the findings discussed in Chapter 4.

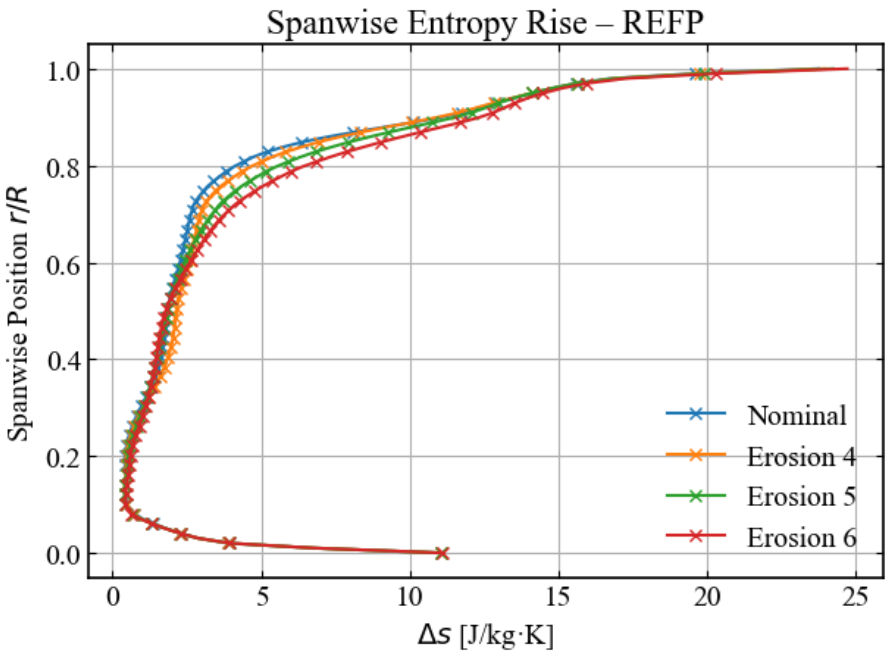

Figure 6.15: Spanwise entropy rise over the rotor blisk for REFP in transonic flow.

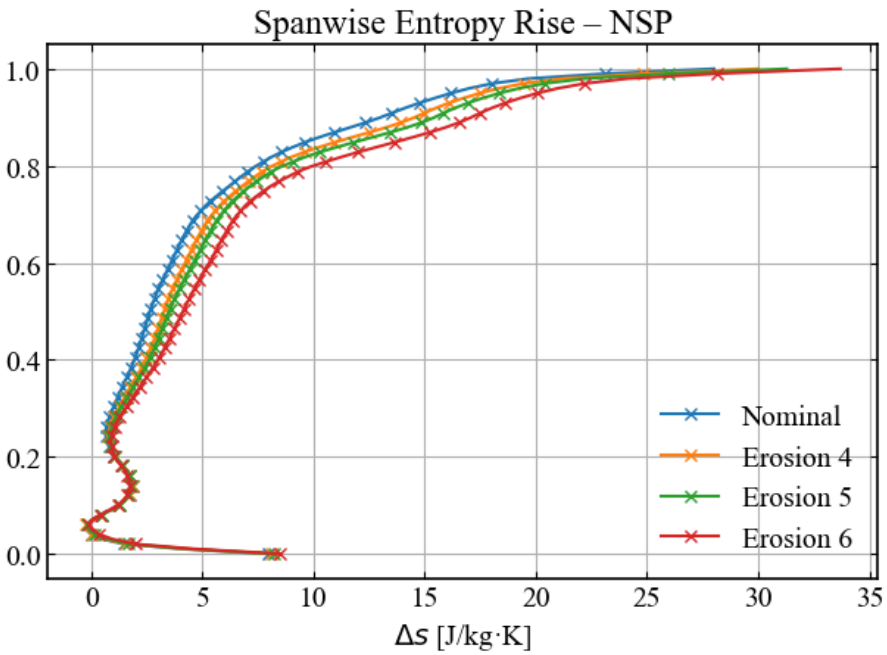

Figure 6.16: Spanwise entropy rise over the rotor blisk for NSP in transonic flow.

At REFP, the most pronounced changes in entropy rise due to increasing erosion severity occur between 70% and 90% span. In contrast, the NSP case shows a broader sensitivity, with increased entropy generation evident from approximately 20% span extending toward the tip. These trends highlight a shift in the loss distribution with erosion severity compared to subsonic conditions, particularly under the REFP operating condition.

Figures 6.17 and 6.18 show the entropy difference between the level 6 eroded and nominal geometries at a spanwise location just downstream of the rotor leading-edge.

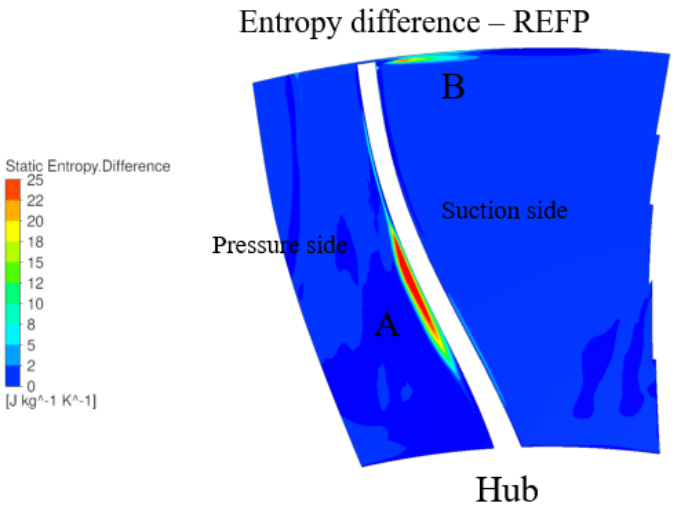

Figure 6.17: Entropy difference (eroded – nominal) at a spanwise location downstream of the rotor leading-edge for REFP.

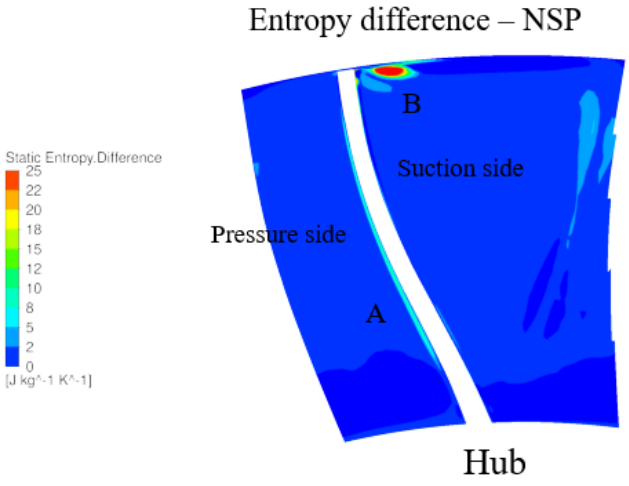

Figure 6.18: Entropy difference (eroded – nominal) at a spanwise location downstream of the rotor leading-edge for NSP.

It can be observed that at point A, for both operatin points a entropy difference region is generated at the pressure side at low to mid spans. This entropy rise is due to a developed seperation region at theses spans, as shown in figure 6.21 and 6.24. Increased local velocity around the leading-edge curvature and the subsequent pressure rise causes increased separation at lower – mid spans on the pressure side for the eroded case, this effect is more pronounced at the reference point. As the flow reattach, a thicker boundary-layer was observed compared to the nominal case.

At point B, entropy increases near the tip region on the suction side, close to the leading-edge, for both operating points. This is likely due to stronger tip-gap effects and the associated losses from increased tip leakage flow and the formation of tip leakage vortices in the eroded case. These effects are driven by higher pressure differences near the tip and are more pronounced at the near stall point.

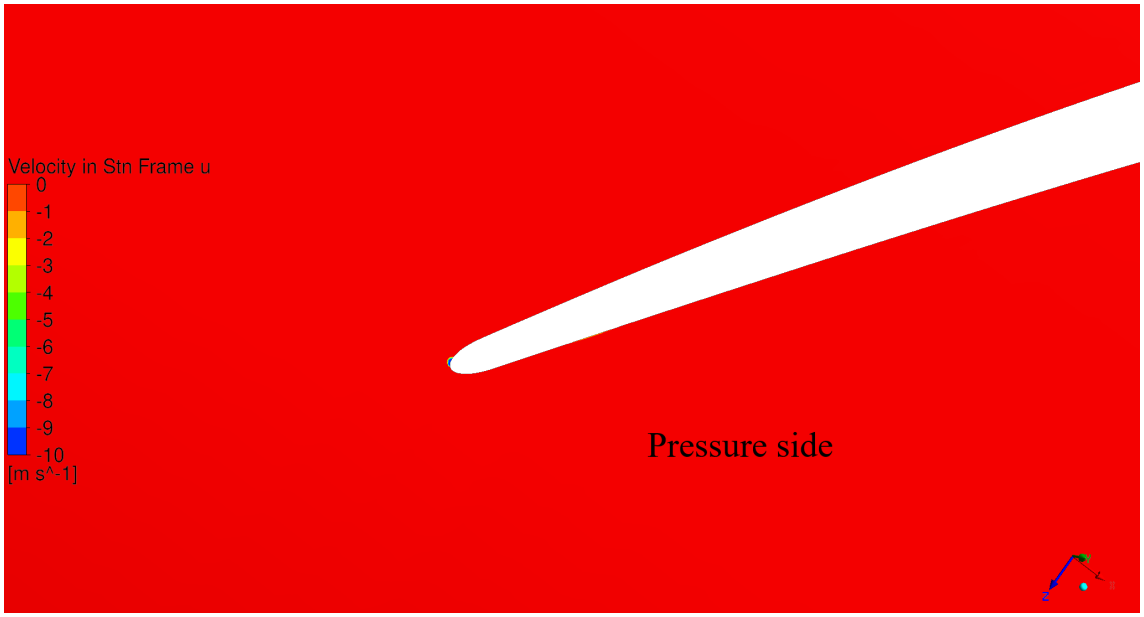

Figure 6.19: Nominal leading-edge.

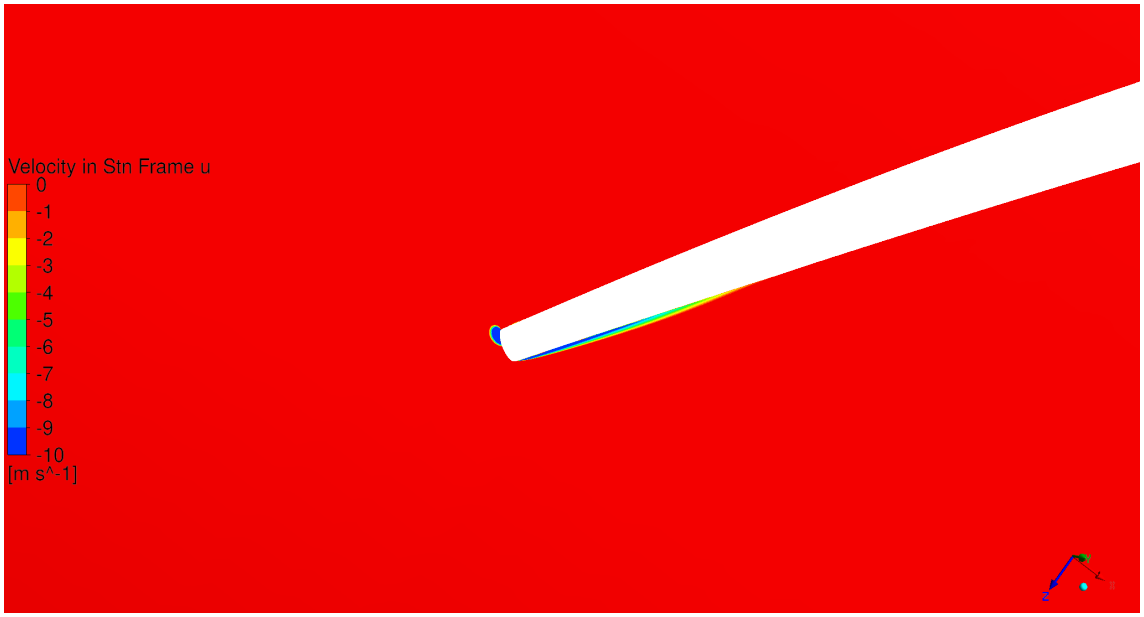

Figure 6.20: Eroded leading-edge.

Figure 6.21: Axial velocity contours at 15% span at REFP for the nominal and eroded blade geometries.

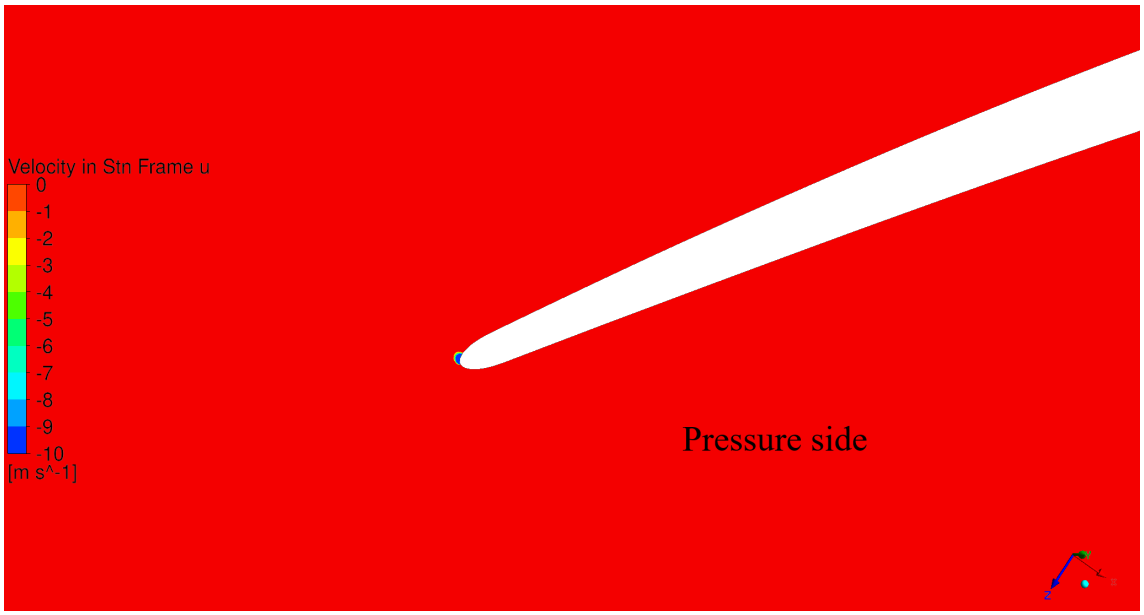

Figure 6.22: Nominal leading-edge.

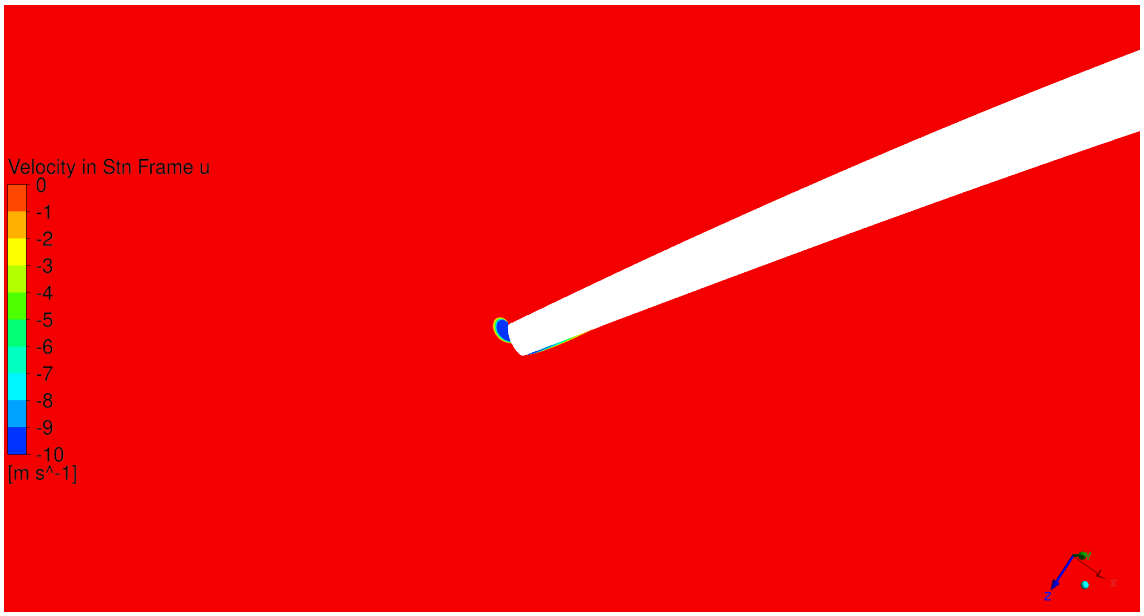

Figure 6.23: Eroded leading-edge.

Figure 6.24: Axial velocity contours at 15% span at NSP for the nominal and eroded blade geometries.

7

Measurable limits (R134a)

This chapter assesses the detectability of erosion effects using synthetic pressure signals under transonic conditions. Static pressure data from steady-state CFD is post-processed to replicate high-frequency sensor outputs. A frequency-domain analysis is conducted to quantify measurable changes across different sensor locations and erosion levels. Measurement limit investigations were conducted exclusively using heavy gas (R134a) under transonic conditions, aligning with the operating conditions of the upcoming rig test campaign. This focused approach ensured consistency with the expected test environment of the Darling NFFP project [16]. Therefore, investigations at subsonic conditions were excluded from this part of the study.

7.1 Method

7.1.1 Pressure Transducer Signal Replication

To replicate the behavior of pressure transducers similar to the Kulite sensors used in the Stuttgart rig, synthetic sensor data was extracted from steady-state CFD simulations. Since time-resolved simulations were not conducted in this study, the static pressure field signals was exported along a circumferential line at a fixed axial position within the theta sector at the shroud casing of the domain.

A virtual sampling frequency of 200,000 Hz was applied to the extracted circumferential data to replicate the temporal resolution of the high-frequency transducer. The data along the circumferential line over one rotating revolution was then post-processed to simulate a time-resolved signal as the rotor blades passed by the sensor probe.

It is important to note that this approach does not account for certain real-world effects such as measurement noise, sensor dynamics, or flow unsteadiness not captured in steady-state solutions. Despite these limitations, the method provides a useful first-order approximation of the spectral content that would be captured by actual Kulite transducers in a experimental setting.

7.2 Steady Effects and Sensor data

7.2.1 Shroud Pressure Field

Figure 7.1 and 7.2 shows a comparison of the static pressure field at the shroud casing trough out the computational domain for both operating points. In the contour plot, grey lines indicate three sensor positions: upstream (SP5), just downstream of the leading edge (SP7), and downstream (SP16).

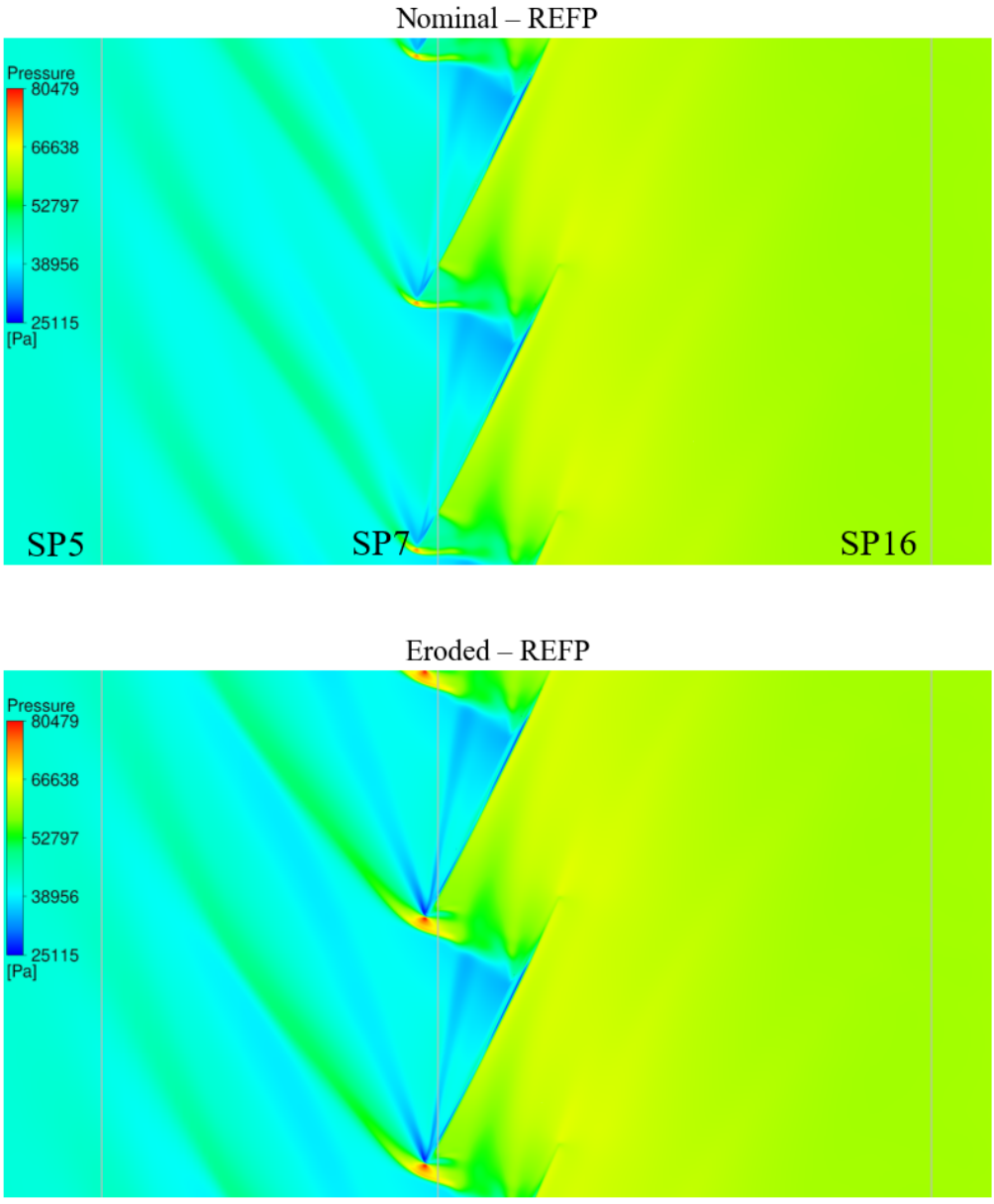

Figure 7.1: Static pressure field at the shroud casing at REFP.

For both the reference point (REFP) and the near-stall point (NSP), the sensors located upstream (SP5) and downstream (SP16) lie in regions where only minor differences in the static pressure field are observed. However, due to the presence

of a stronger and slightly shifted bow shock at both operating points, the upstream sensor (SP5) appears to cross a in a slightly larger high-pressure zone caused by shock-induced compression.

The sensor positioned just downstream of the leading edge (SP7) lies in a region where the pressure field exhibits more pronounced differences between the nominal and eroded case. Following the grey line at SP7 from top to bottom in the figure, the sensor is situated in a region of lower static pressure, which is attributed to the trace of the tip-leakage vortex traversing the blade passage and the low-pressure zone over the rotor tip gap. Additionally, the sensor also passes through a region of increased static pressure, associated with a stronger and slightly shifted bow shock forming in front of the blade.

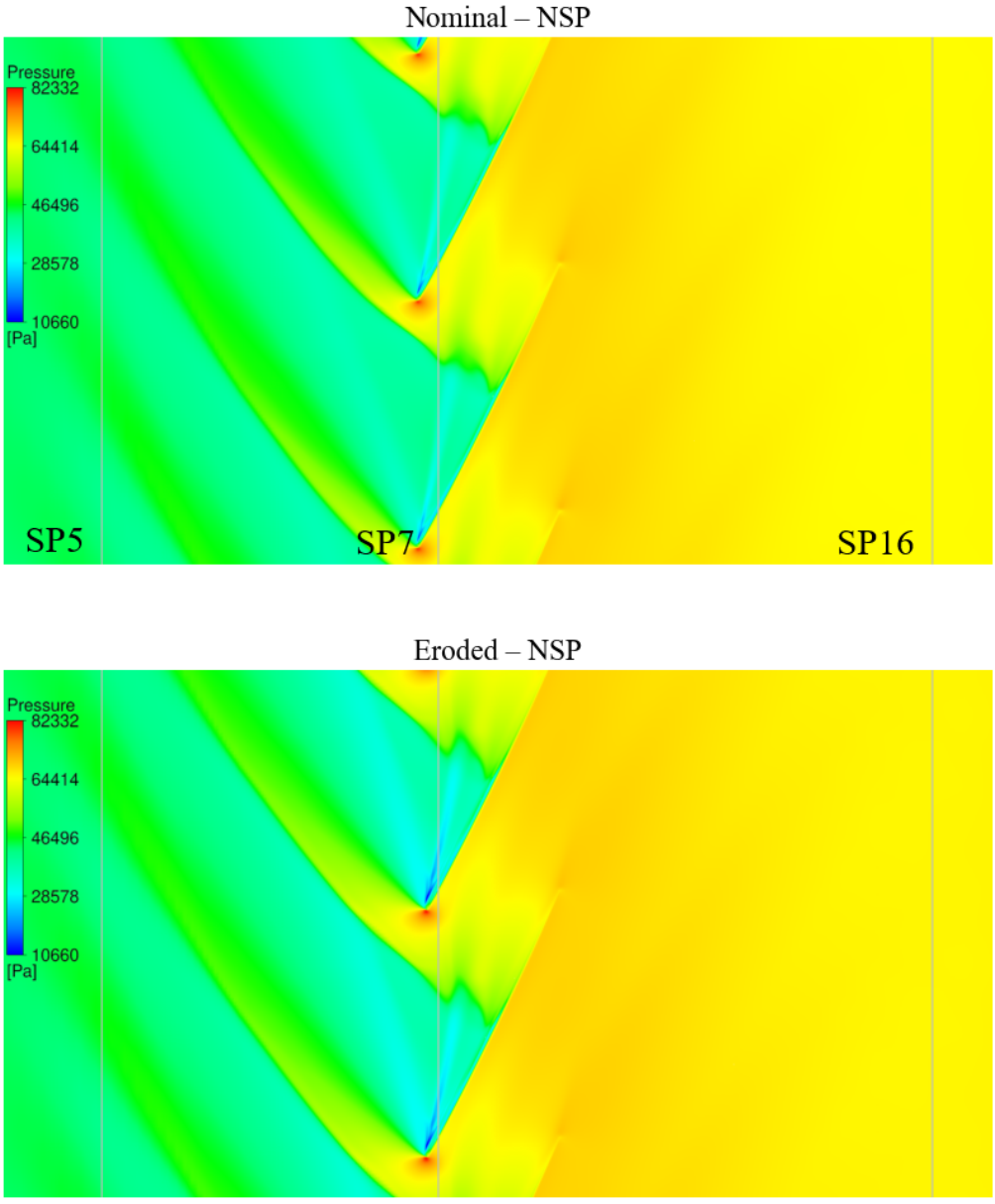

Figure 7.2: Static pressure field at the shroud casing at NSP.

7.2.2 Frequency-Domain Analysis (FFT)

To analyze the differences and changes in characteristics of the static pressure signal between the nominal and eroded cases, the time-domain signal is converted to the frequency domain using a Fast Fourier Transform (FFT). This is shown in Figures 7.3 and 7.4, where the first five blade passing frequencies (BPFs) are compared by evaluating the absolute difference in amplitude between each eroded case and the nominal signal, based on the highlighted sensor positions in Figures 7.1 and 7.2.

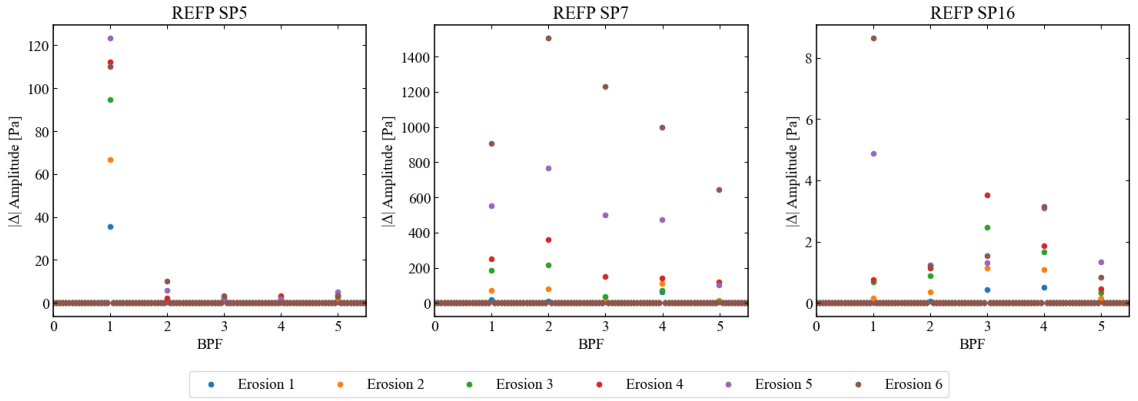

Figure 7.3: Absolute amplitude differences at the first five blade passing frequencies (BPFs) between the nominal and eroded cases at SP5, SP7, and SP16 for REFP.

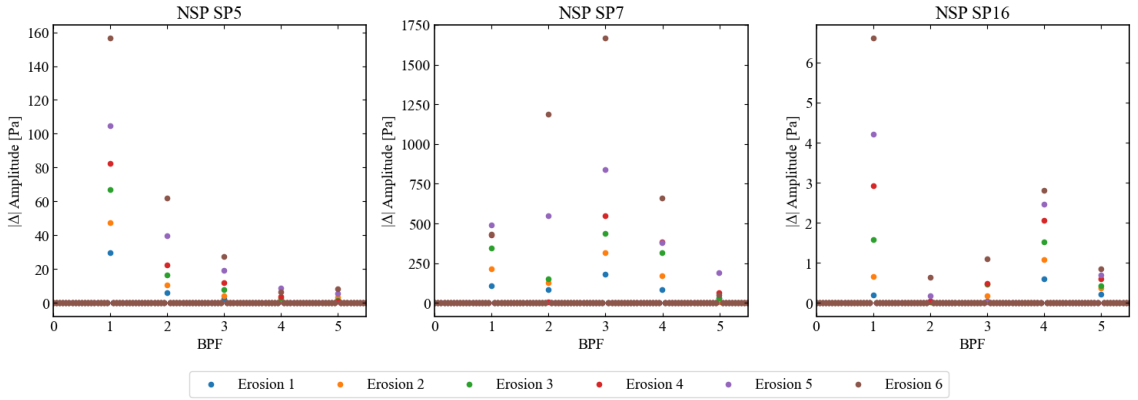

Figure 7.4: Absolute amplitude differences at the first five blade passing frequencies (BPFs) between the nominal and eroded cases at SP5, SP7, and SP16 for NSP.

The figure shows that, at the first BPF, the amplitude—corresponding to one blade passing the sensor—has changed for all erosion cases at all sensor positions(SP5, SP7 and SP16) and for both operating points. This indicates that erosion affects the fundamental pressure signal at all three locations. The smallest change in amplitude at the first BPF is observed at the downstream sensor (SP16) for both operating points.

Focusing on the sensor positioned just downstream of the leading edge (SP7), the largest absolute difference in amplitude is observed at frequencies above the first BPF when compared to the upstream (SP5) and downstream (SP16) sensors. This

is likely due to SP7 being located in a region of the flow field that experiences stronger shock dynamics and more pronounced tip-gap interactions. These effects are consistent with the pressure field observations shown in Figures 7.1 and 7.2, where the tip-leakage and subsequent tip-leakage vortex, and shifting shock structure are more dominant in this region.

7.2.3 Measurable Limits

Figure 7.5 illustrates the axial distribution of all sensors along the shroud casing, indicated by the plot markers.
To investigate the measurable limits of the static pressure field along the shroud casing, additional sensors have been added beyond those shown in Figure 4.9. The x-axis in Figure 7.5 represents the chord-normalized axial coordinate at various blade passing frequencies (BPFs). Key axial positions are marked with dashed lines, including the trailing edge of the inlet guide vane (IGV), the rotor leading and trailing edges (LE and TE), and the stator leading edge.

An estimated minimum required amplitude difference for detection, set at 20 Pa, is indicated by a green horizontal dashed line. It can be observed that, in terms of detectability, the region just upstream of, at, and just downstream of the rotor leading edge captures the strongest erosion signature at lower frequencies (BPF 1–3) for both operating points. At these frequencies, the results appear predictable: as erosion severity increases, the amplitude difference also increases at most sensor positions. Most sensors in this region are able to detect an absolute difference well above the minimum threshold across all erosion cases.

Detectability decreases significantly beyond approximately 70% of the axial chord length, where most sensor positions fall below the detection threshold for all erosion levels.

At higher frequencies (BPF 15 and BPF 20), detectability declines rapidly outside the region above the rotor. Additionally, the relationship between erosion severity and amplitude difference becomes less consistent compared to lower frequencies, making it more difficult to predict how increasing erosion affects the pressure signal amplitude.

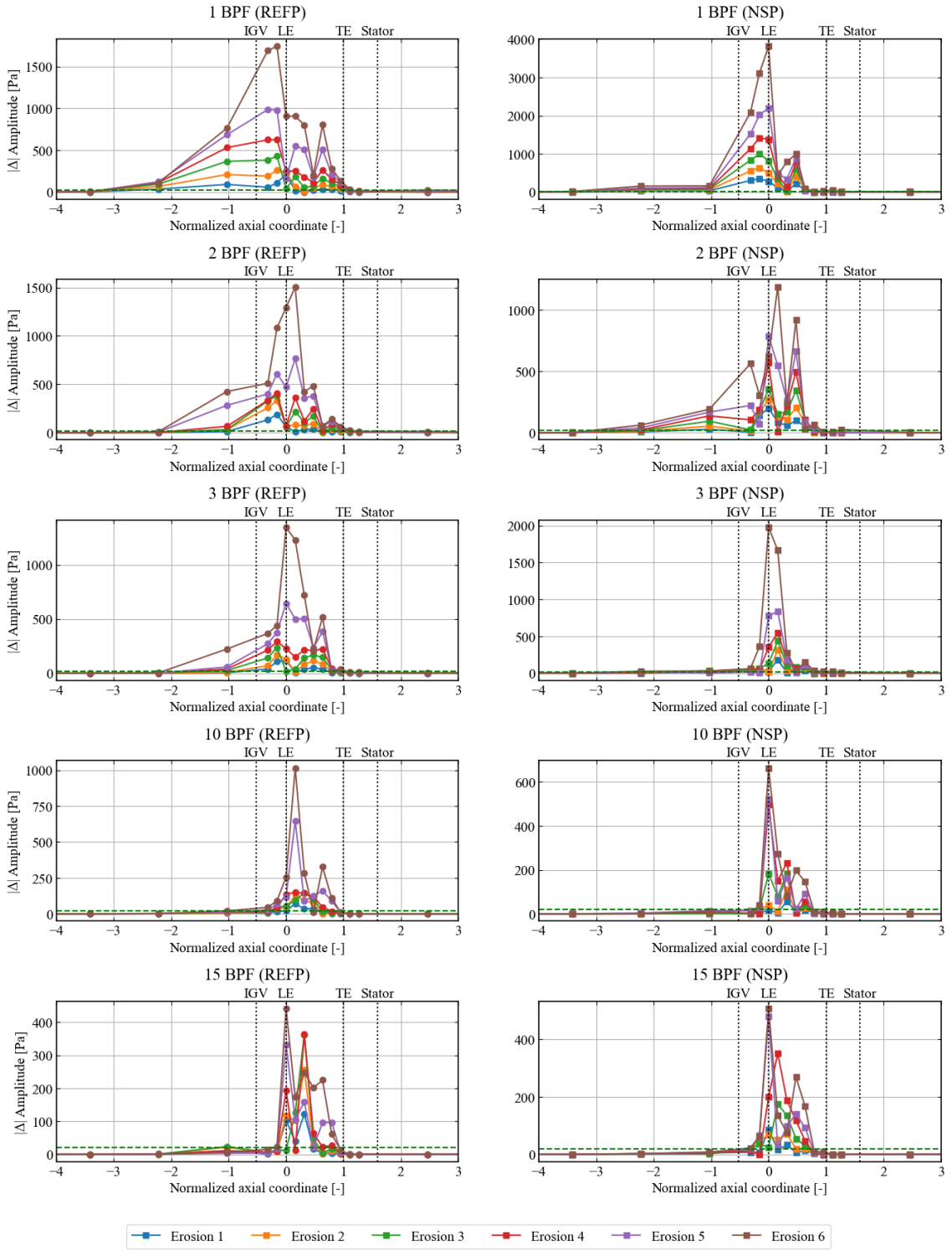

Figure 7.5: Axial distribution of the absolute pressure amplitude difference between nominal and eroded cases.

8

Comparative Analysis and Conclusions

8.1 Aerodynamic Impact: Subsonic vs. Transonic Erosion

This study investigated the aerodynamic impact of leading-edge erosion under both subsonic and transonic flow conditions. The results from both cases suggest that increased erosion severity negatively affects multiple aspects of rotor performance. While both flow regimes showed a comparable reduction in polytropic efficiency, it is important to note that this outcome was only achieved in the transonic case by increasing the erosion severity by a factor of four. This implies that transonic rotors may be inherently less sensitive to moderate erosion—requiring more severe damage before a comparable performance drop in polytropic efficiency is observed compared to subsonic conditions.

A detailed loss analysis reveals that the erosion-induced loss mechanism differs between the two flow regimes. In the subsonic case, erosion primarily increased entropy generation near the blade tip. This was attributed to a combination of an enlarged separation bubble on the suction side at this region, and a increased tip-gap leakage. In contrast, for the transonic case, an additional contribution to performance loss stemmed from a shifting structure of the shock system. The erosion-induced blunting and reduced chord at the leading edge appears to straighten and shift the shock structure, degrading aerodynamic performance and increasing entropy production.

8.2 Erosion Monitoring Recommendations

All analyses and recommendations presented in this section are based on simulations conducted using heavy gas (R134a) under transonic conditions. Consequently, investigations under subsonic conditions were not included.

8.2.1 Spatial and Spectral Sensitivity

In terms of spatial sensitivity, the leading-edge region—extending roughly half an axial chord upstream and downstream—captures the strongest erosion signatures. A sensor located at or just downstream of the rotor leading edge consistently records

the largest pressure deficit, making it the most informative position.

Beyond approximately 70% of the axial chord, signal strength decays rapidly and only weak trends with erosion severity are preserved. Consequently, sensors placed downstream of the rotor trailing edge contribute little value, as amplitude differences rarely exceed the 20 Pa detection threshold.

Spectrally, the low harmonics (BPF 1–3) within the same axial window—spanning half a chord length upstream and downstream, from the rotor leading-edge—correlate with erosion severity, showing a clear, monotonic increase in amplitude difference. These low harmonics (BPF 1–3), suggest to be the most reliable indicators of leading-edge erosion under steady-state conditions.

At higher harmonics ($\geq$ BPF 10), signal variation becomes irregular and sensitive to sensor placement, with detectability generally falling below the threshold. As a result, these frequencies are not recommended for primary erosion monitoring.
The spectral trends hold across both operating points—reference (REFP) and near-stall (NSP)—with NSP showing a slightly narrower region of detectability downstream of the leading edge at BPF 1 and 3. This confirms that the proposed monitoring strategy remains robust even under moderate off-design conditions.

8.2.2 Recommended Erosion Levels for Experimental Validation

All erosion severities examined in this study are theoretically detectable within a narrow window of approximately ± 0.2 axial chord around the rotor leading edge, based on BPF 1–3 under the delta measurement threshold (20 Pa). To account for uncertainty in sensor placement and the true measurement threshold, the threshold envelope is suggested by the author to be extended to span one axial chord upstream and one-half chord downstream with respect to the suggest delta measurement threshold (20 Pa).

Based on this analysis, the following two erosion severities are recommended for experimental validation:

- **Erosion Level 3 ($\approx 1\%$ chord reduction at the tip):** This case lies just above the 20 Pa detection threshold at one axial chord upstream and one-half chord downstream. It serves as a stringent test case for sensor capability at the lower detectability limit.
- **Erosion Level 5 ($\approx 3\%$ chord reduction at the tip):** This level is comfortably above the threshold across the entire threshold envelope and is expected to produce clear, repeatable pressure signals—ideal for validating trend robustness.

Together, these cases provide a balanced test scenario: one probing the edge of sensor sensitivity and the other offering a high-confidence reference based on the

results of this study.

Recommended Blade Arrangement for the 18-Blade Rotor

Given the rotor's 18-blade configuration, an efficient way to test erosion levels on a single blisk is to divide the rotor into two alternating group types, as illustrated in Figure 8.1.

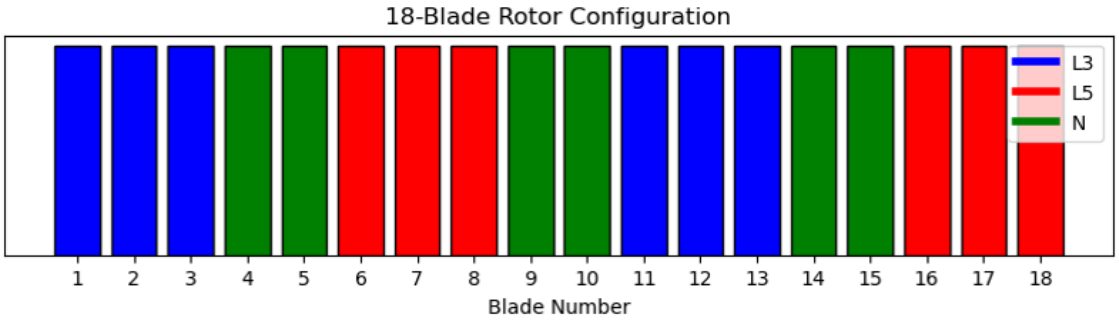

Figure 8.1: Suggested alternating 18-blade configuration for erosion testing.

Blade Group Definitions:

- **Eroded Blade Group:** Contains 3 blades with the same erosion level (either L3 or L5).
- **Nominal Blade Group:** Contains 2 blades with no erosion (Nominal).

Testing Benefit:

- This configuration enables testing of eroded blades both in adjacent positions and separated by nominal blades, providing insight into interaction effects and spatial sensitivity.

8.3 Limitations and Future Work

While the study offers robust findings under steady-state assumptions, several limitations should be addressed in future work:

- **Blade configuration validation:** Investigate the effects of the proposed 18-blade configuration. A full 360° simulation prior to the "go-ahead" of manufacturing could potentially provide additional insight into the aerodynamic implications and measurable information.
- **Boundary-layer transition modeling:** Include laminar-to-turbulent boundary-layer transition effects in future investigations, as these transition effects have been observed to influence the flow field behavior due to erosion in previously conducted studies.
- **Unsteady effects:** All results are derived from steady-state simulations. Transient simulations are necessary to capture real-time dynamics such as vortex shedding, shock oscillation, and tip-leakage fluctuations, which potentially could provide additional information.

- **Erosion morphology:** This investigation considered only leading-edge blunting and chord reduction. Future work should explore alternative damage modes (e.g., delta twist, increased tip-gap clearance, or surface roughness) to assess the generalizability of rotor blade damage effects.
- **Manufacturing and rig integration:** Practical aspects of implementing synthetic erosion, such as tolerance control, balancing, and repeatability, must be evaluated before finalizing an experimental campaign.

Bibliography

[1] Shi, L., Guo, S., Yu, P., Zhang, X., & Xiong, J. (2023). *A Review on Leading-Edge Erosion Morphology and Performance Degradation of Aero-Engine Fan and Compressor Blades*. Energies, 16(7), 3068. https://www.mdpi.com/1996-1073/16/7/3068. DOI: 10.3390/en16073068.

[2] Boyce, M. P. (2012). *3 - Compressor and Turbine Performance Characteristics*. In M. P. Boyce (Ed.), *Gas Turbine Engineering Handbook* (4th ed., pp. 139–176). Butterworth-Heinemann, Oxford. https://www.sciencedirect.com/science/article/pii/B9780123838421000032. DOI: 10.1016/B978-0-12-383842-1.00003-2.

[3] Howell, A. R. (1945). *Fluid Dynamics of Axial Compressors*. Proceedings of the Institution of Mechanical Engineers, 153(1), 441–452. https://doi.org/10.1243/PIME_PROC_1945_153_049_02. DOI: $10.1243/\mathrm{PIME}_{P}ROC_{1}945_{1}53_{0}49_{0}2$.

[4] Korpela, S. A. (2011). *Principles of Turbomachinery* (1st ed.). John Wiley & Sons, Incorporated, New York. https://library.chalmers.se/. Note: Accessed via Chalmers Library E-book Collection.

[5] Kappis, W. (2012). *Detailed compressor degradation effect modeling for single blade rows while assessing its local and overall consequences*.

[6] Hamed, A., & Tabakoff, W. (1994). *Experimental and numerical simulations of the effects of ingested particles in gas turbine engines*. In *AGARD Conference Proceedings AGARD CP* (pp. 11–11). AGARD.

[7] Diakunchak, I. S. (1992). *Performance Deterioration in Industrial Gas Turbines*. Journal of Engineering for Gas Turbines and Power, 114(2), 161–168. https://doi.org/10.1115/1.2906565. DOI: 10.1115/1.2906565.

[8] Ma, D., Harvey, T. J., Wellman, R. G., & Wood, R. J. (2019). *Characterisation of rain erosion at ex-service turbofan blade leading edges*. Wear, 426–427, 539–551. 22nd International Conference on Wear of Materials. https://www.sciencedirect.com/science/article/pii/S0043164818316430. DOI: 10.1016/j.wear.2018.12.050.

[9] Roberts, W. B., Armin, A., Kassaseya, G., Suder, K. L., Thorp, S. A., & Strazisar, A. J. (2002). *The Effect of Variable Chord Length on Transonic Axial Rotor Performance*. Journal of Turbomachinery, 124(3), 351–357. https://doi.org/10.1115/1.1459734. DOI: 10.1115/1.1459734.

[10] Stein, T., Leitner, M. W., & Staudacher, S. (2024). *Effect of Leading Edge Erosion on the Tip Leakage Flow in a Compressor Cascade*. Journal of Turbomachinery, 1–10. https://doi.org/10.1115/1.4067462. DOI: 10.1115/1.4067462.

[11] Tabakoff, W. (1988). *Causes for Turbomachinery Performance Deterioration*. In *Volume 1: Turbomachinery*, Turbo Expo: Power for Land, Sea, and Air (pp. V001T01A104). https://doi.org/10.1115/88-GT-294. DOI: 10.1115/88-GT-294.

[12] Chirayath, E., Xu, H., Yang, X., & Kunz, R. (2023). *Full Stage Axial Compressor Performance Modeling Incorporating the Effects of Blade Damage Due to Particle Ingestion*. Journal of Turbomachinery, 145(9), 091001. https://doi.org/10.1115/1.4062397. DOI: 10.1115/1.4062397.

[13] Yu, X., Zhao, S., An, G., Xu, Y., & Xu, X. (2023). *Experimental Investigations on the Effects of Surface Roughness for Compressor Cascades With Different Roughness Magnitude and Location*. Journal of Turbomachinery, 146(3), 031007. https://doi.org/10.1115/1.4063973. DOI: 10.1115/1.4063973.

[14] Tabakoff, W., Lakshminarasimha, A. N., & Pasin, M. (1990). *Simulation of Compressor Performance Deterioration Due to Erosion*. Journal of Turbomachinery, 112(1), 78–83. https://doi.org/10.1115/1.2927424. DOI: 10.1115/1.2927424.

[15] Goodhand, M. N., & Miller, R. J. (2010). *Compressor Leading Edge Spikes: A New Performance Criterion*. Journal of Turbomachinery, 133(2), 021006. https://doi.org/10.1115/1.4000567. DOI: 10.1115/1.4000567.

[16] KTH Energy Technology. (2025). *DARLING - Damaged and Repaired Blade Modeling with in-situ Experiments*. https://www.energy.kth.se/heat-and-power-technology/current-projects/darling-damaged-and-repaired-blade-modeling-with-in-situ-experiments-1.1369396. Accessed: 2025-03-27.

[17] DesignGyan. (2025). *CFX-Pre: A Comprehensive Guide*. https://designgyan.com/srp457/assets/images/papers/DG_09444062_cfxpre.pdf.

[18] Anderson, J. D. (2010). *Fundamentals of Aerodynamics* (5th ed.). McGraw-Hill Education. https://onlinelibrary.wiley.com/doi/pdf/10.1002/9781118534786.app1.

[19] Buchwald, P., Müller, F. F., Günther, M., & Vogt, D. M. (2024). *A New Axial Compressor Test Facility for the Investigation of Aerodynamic Damping Featuring an Electromagnetic Excitation System*. Journal of Turbomachinery, 146(7), 071006. https://doi.org/10.1115/1.4065241. DOI: 10.1115/1.4065241.

[20] Wikipedia contributors. (2024). *Axial compressor — Wikipedia, The Free Encyclopedia*. https://en.wikipedia.org/wiki/Axial_compressor. Accessed: 2025-05-19.

[21] Wikipedia contributors. (2025). *Compressor map — Wikipedia, The Free Encyclopedia*. https://en.wikipedia.org/wiki/Compressor_map. Accessed: 2025-05-19.

[22] Kulite Semiconductor Products, Inc. (2025). *Kulite Reference Library*. https://kulite.com/technology/reference-library/. Accessed: 2025-05-19.

[23] Gambini, M., & Vellini, M. (2021). *Fundamentals of Thermodynamics and Fluid Dynamics of Turbomachinery*. In *Turbomachinery: Fundamentals, Selection and Preliminary Design* (pp. 1–88). Springer International Publishing, Cham.

https://doi.org/10.1007/978-3-030-51299-6_1. DOI: 10.1007/978-3-030-51299-6_1.

[24] Lampart, P. (2006). *Tip leakage flows in turbines*. TASK Quarterly, 10, 139–175.

DEPARTMENT OF MECHANICS AND MARITIME SCIENCES
CHALMERS UNIVERSITY OF TECHNOLOGY
Gothenburg, Sweden
www.chalmers.se

CHALMERS
UNIVERSITY OF TECHNOLOGY